Deliverable

D4.5
The use of structural health monitoring for rapid loss assessment

Deliverable information	
Work package	WP4 Effects
Lead	[Institution]
Authors	Dr. Yves Reuland, IBK-ETH Panagiotis Martakis, IBK-ETH Prof. Eleni Chatzi, IBK-ETH
Reviewers	[Iunio Iervolino, UNINA Pasquale Cito, UNINA Eugenio Chioccarelli, UNINA]
Approval	[Management Board]
Status	Final
Dissemination level	[internal]
Delivery deadline	31.08.2022
Submission date	[31.08.2022]
Intranet path	[DOCUMENTS/DELIVERABLES/File Name]

This project has received funding from the European Union's Horizon 2020 research and innovation programme under grant agreement No 821115

Table of contents

Summary

Within the RISE work package 4.4, the application of Structural Health Monitoring (SHM) to near-real-time post-earthquake damage assessment of buildings is investigated. In absence of means to measure damage directly, continuously monitored data, such as accelerations, which are indirectly linked to damage, are processed in order to answer the questions: is the building *safe* for occupancy (green tag)? Is damage expected in the building (amber tag)? Is the probability of extensive damage significant and the building should be *evacuated* (red tag)?

A set of damage-sensitive features (DSFs) that can be extracted from measured acceleration signals has been developed to detect onset of damage. DSFs correlate with the amount of nonlinearity a structure is exposed to and the related structural degradation. Combined with a physics-based (engineering) model, DSFs contain information regarding the damage state of a building. In addition, the statistical treatment of DSFs enables tracking the accumulation of building damage over time, reducing the need for repeated inspections during seismic sequences.

Bridging the gap between building-specific information that stems from monitoring data and approximate building models for regional damage and loss estimation, pre-defined damage-state probabilities with respect DSFs are formulated in a similar manner to classical fragility curves.

The use of DSF-based fragility curves and data-driven damage detection is demonstrated for a case study on data from a shaking-table and the coding and evaluation of key steps is offered in an accompanying html demonstrator (https://yreuland.github.io/SHM_Demonstrator/SHM_Demonstration_RISE.html). The successful tagging of the building – in agreement with observations made on the tested specimen – underlines the potential of SHM to reduce uncertainties in post-earthquake damage assessment and accelerate building tagging, thus increasing the resilience of European communities with respect to damaging earthquakes.

1. Introduction into SHM

The enforcement of modern building design codes and the evolution of construction techniques have contributed to reducing seismic risk. However, modern seismic design criteria for residential buildings focus on life safety of building occupants with performance-based earthquake engineering geared toward tolerating damage under strong ground motions. Therefore, earthquakes will continue to threaten the integrity of the built environment and trigger post-earthquake damage and loss assessment. As not all buildings react in the same way to earthquake actions, a rapid understanding of the extent of damage to buildings and its consequences on providing safe shelter for the population is a crucial contribution to an earthquake-resilient Europe. Currently, post-earthquake assessment of buildings relies on expert-conducted visual inspections that, despite being increasingly standardized, suffer from possible subjectivity (Galloway et al., 2019) and delay rapid recovery due to the time required to inspect large building stocks (Mcentire & Cope, 2004).

However, recent advances in sensor development have resulted in an increasing availability of sensing hardware at low cost, thus making permanent installations of sensors a realistic outlook, even for conventional buildings that form the largest portion of the existing building stock. Structural health monitoring (SHM) offers the tools to analyze such a permanent inflow of sensor data and retrieve information regarding the structural state (health) of the structure. In the absence of means for direct measurements of building damage, indicators of damage need to be derived from indirect measurements, such as accelerations.

Traditionally, the correlation between the stiffness of a structure and the vibration modes has been leveraged and therefore, many applications of SHM for the built environment rely on changes in vibrational properties to extract indicators of damage (Carden & Fanning, 2004; Salawu, 1997). Changes in natural frequencies or damping coefficients have been linked with damage (Basseville

et al., 2004; Gentile et al., 2016a; Lorenzoni et al., 2018; Vidal et al., 2014), while mode shapes or mode-shape curvature have been found to be correlated with the location of damage (Giordano et al., 2021; Giordano & Limongelli, 2020; Shokrani et al., 2018).

However, relying on data alone often proves insufficient. Fully data-driven classification of damaged buildings into categories that indicate damage severity would, for instance, require large datasets to derive – or train – the thresholds that are required for damage classification, either based on statistical damage detection or machine-learning (ML) applications (Avci et al., 2021), which need to feed on relevant seismic response data. Yet, historic monitoring data of earthquake-damaged buildings are scarce. In complementing the needed information, physics-based models can be employed to refine the identification potential in terms of sharpening detection and hinting to localization (Jaishi & Ren, 2006; Kaya et al., 2015; Kita et al., 2021). The two aforementioned tasks comprise only the first two levels of damage identification (Rytter, 1993), and do not typically entail a quantification of damage (third level), which may then lead to remaining useful life assessment (fourth level). In achieving these higher-end tasks, model-based SHM is typically required (Trevlopoulos & Guéguen, 2016), but often entails the use of computationally expensive and structure-specific models (Atamturktur & Laman, 2012; Kita et al., 2020; Reuland et al., 2019a, 2019b).

In this work, we exploit a hybrid approach which capitalizes on the fusion of monitoring data from few monitored instances and physics-based models for automated building tagging. We propose a framework based on DSFs to assess the presence of damage and – by comparison to DSF-based fragility curves that are previously simulated – enables a probabilistic attribution of building tag. This approach can be employed for single buildings, yet, given the formulation of fragility functions, is also compatible with regional post-earthquake loss and damage assessment.

Integration within the RISE project

SHM for rapid post-earthquake damage assessment offers numerous synergies with other RISE objectives. Although the demonstrator that is provided here is focused on a single building, the formulation of the seismic SHM framework offers the flexibility for application at regional scale. Reducing the uncertainty from simplified regional loss assessment methodologies through monitoring data – possibly combined with methodologies to use information from a small subset of buildings to reduce the regional loss-assessment uncertainty, as proposed within task 4.3 (Bodenmann et al., 2021; Reuland et al., 2022) – benefits rapid-loss assessment (task 4.1) and prediction of regional repair-and-recovery efforts (task 4.3). The regional application of SHM for building tagging will be further investigated in collaboration with task 6.1.

SHM modules can readily signal damage detection, with more refined algorithms taking on the assessment of localization and severity of damage. However, post-earthquake decision-making ideally also assesses the influence of damage and its accumulation on the vulnerability of buildings in their post-earthquake state to deduce the state-dependent risk of its inhabitants. State-dependent fragility curves, such as those proposed in task 4.2, may be combined with SHM-based prediction of damage states to reduce the uncertainty of the fragility of damaged buildings after earthquakes.

In addition to reducing uncertainties and thereby improving post-earthquake decisions, SHM has the potential to significantly reduce the downtime related to post-earthquake assessment of buildings: accelerating the attribution of green tags – corresponding to safe buildings – from several days or even weeks, as is the case for lengthy visual inspections, to minutes, as could be the case with automated building tagging, may, for instance, be a crucial contribution towards earthquake-resilient communities. Together with task 4.6, we will shed light on the tradeoff between these benefits and the cost of structural health monitoring.

2. Framework for near-real-time data-driven damage tagging

Automated near-real time tagging of buildings after earthquakes requires information on the damage that has been sustained during the earthquake. Several methodologies can be followed for damage assessment and building tagging at regional scale, with an overview offered in Figure 1.

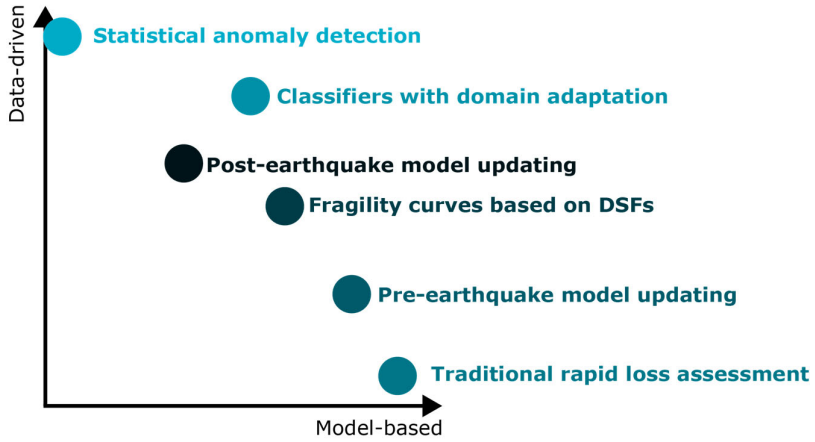

Figure 1 A classification of methodologies for post-earthquake damage assessment.

Traditional rapid loss assessment relies on shake-maps that are derived from seismic network stations (Wald et al., 1999), which may form a dense network in regions with high seismic hazard, such as central Italy, but are coarsely spaced in regions with low-to-moderate seismicity. As a result, the intensity measure at the exact location of buildings is often not available, yet an estimate may be computed (Worden et al., 2018). The uncertainties underlying such estimates undermine decision-making, when seismic network stations are scarce (Bodenmann et al., 2022). Moreover, while rapid loss assessment heavily relies on model-based predictions, the regional scope of this methodology does not offer precise predictions for individual buildings, as the approximate nature of both intensity measures and building models is intended for loss predictions that are aggregated over hundreds of buildings.

As demonstrated in published work related to this task, pre-earthquake monitoring data can be used to reduce the uncertainties in fragility functions that are used for traditional rapid loss assessment (Martakis, Reuland, Imesch, et al., 2022). However, the uncertainty reduction only affects the material and model parameters of engineering models used to derive fragility curves and thus, does not reduce the uncertainties that are inherent to the shake map. The regional fit of generic fragility curves – often established for country-wide or continental validity – may also be improved together with the precision and accuracy of shake-maps by leveraging small subsets of inspected buildings after a damaging earthquake (Bodenmann et al., 2021). While this reduced the time required for reliable loss assessment from weeks to days, it does not provide near-real time estimates.

The ever-increasing computational power has enabled the use of ML and deep learning applications (Avci et al., 2021) for transforming raw data or DSFs into damage classes, for instance to differentiate healthy and damaged monitoring data or even perform classification of buildings into various classes of damage severity of damage (Hoelzl et al., 2022; Sun et al., 2020; Tsuchimoto et al., 2021). However, supervised ML approaches require large amount of labelled data and thus, cannot be directly applied to the classification of buildings after earthquakes, given the lack of historic monitoring data from earthquake-damaged buildings. Owing to this lack of data, relying on a limited number of inspected buildings for damage assessment at larger scales has been proposed as an alternative to overcome the lack of historic labelled data (Bodenmann et al., 2021; Mangalathu et al., 2020; Sheibani & Ou, 2021, 2022; Stojadinović et al., 2022).

Another approach to overcome the scarcity of real-world data of damaged structures, is to rely on model simulations (Movsessian et al., 2022; Xu & Noh, 2019). However, engineering models contain inherent bias and multiple sources of uncertainty that prevent the realistic representation of the measured response. A remedy to this can be sought in transfer learning; a ML technique, which aims to transfer knowledge from a source domain, where a large amount of labeled data is available, to a target domain, with very limited labeled data (Pan & Yang, 2010). Domain adaptation addresses this task by reducing the distance between the data distributions of the source and the target domains and increases the performance by capitalizing on population-based SHM (Bull et al., 2021).

Post-earthquake updating of physics-based models with building-specific monitoring data may reduce the uncertainty of model parameters (Reuland et al., 2019). Yet, it requires large amount of model simulations and provides building specific information. While such an approach may be suitable for buildings with a prominent role in post-earthquake responses, such as community centers, schools, and civil-protection offices, its applicability to regional loss assessment is limited.

Statistical anomaly detection is fully data-driven and does not require a physics-based model. Such data-driven damage detection rather relies on the deviation between healthy reference data and data that characterizes the building behavior during an earthquake. While such data-driven methods are helpful in detecting the onset of damage and even provide information about the evolution of the severity of damage – as will be explained in Section 4.1 – they may be insufficient to tag the buildings based on the lacking correlation between amount of damage and its physical meaning. Indeed, typically accelerations are measured and thus, the DSFs that may be derived are not directly linked with properties that are used to quantify damage and its influence on the building capacity, such as stiffness, strength, nonlinearity, and deformation capacity.

As part of Task 4.4 of the RISE project, we propose an approach that is compatible with current regional seismic risk and loss estimation process, namely an approach based on fragility functions. With such a method, probabilities of exceeding pre-defined damage states are evaluated with the help of a physics-based simulators exploiting characteristic building typologies. However, unlike typical fragility functions, the probability of exceeding pre-defined damage states are not expressed as a function of intensity measures (IMs), which only characterize the ground-motion intensity at the base of a building, but as a function of DSFs, which contain critical information on structural condition.

A schematic representation of such a framework is shown in Figure 2.

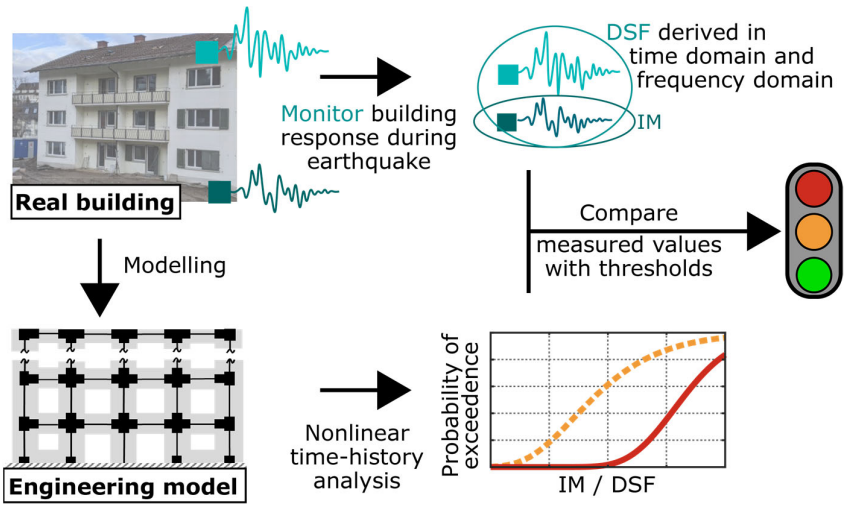

Figure 2 Methodology for near-real time building tagging based on pre-simulated fragility curves. These fragility curves are formulated with respect to measurable DSFs.

Data-driven building tagging relies on the availability of permanently monitored buildings. The rapid processing of dynamic sensor data (i.e., acceleration time series) enables near-real-time estimates of the damage state. DSFs, as elaborated in the next section, can be derived from the measured time series to assess the presence and severity of damage.

The contrasting of monitoring-derived DSFs against thresholds, which can be data-driven or model-defined, allows to tag a building via labels that reflect discrete damage states (Sivori et al., 2022). A convenient way to represent such a tagging is via use of a Red-Amber-Green (RAG) alert system, which can be used to for instance signal evacuation (red), damage (amber), and an undamaged, safe for occupancy (green), state. Damage-tag probabilities can be formulated in a manner similar to classical fragility functions that link the probability of exceeding damage-states to IMs, as shown in Figure 2. Following the fragility functions formulation, IMs which only contain information about the ground-motion, are replaced with DSFs, thus contributing with monitoring-derived information on structural state.

Primary instances of DSFs that are particularly targeted at quantification of seismic-induced damage in building structures are reviewed in the following Section 3 and evaluated with respect to their correlation with engineering-demand parameters and their robustness to noise.

Then, in Section 4 the application of near-real-time building tagging is demonstrated on an experimental case study. Owing to the potentially limited realism of model simulations, when compared to real building behavior, Section 5 contains a proposal to adapt a pre-trained damage classifier with limited *healthy* data from permanently monitored buildings.

3. Damage-sensitive features

Exploiting the increasing availability and decreasing costs of sensor technologies that allow for measurement of building vibration response, the use of modal properties – mostly derived from ambient vibrations – has been shown to carry information which allows to detect structural damage (Akhlaghi et al., 2021; Lorenzoni et al., 2018; Ou et al., 2016; Vidal et al., 2014). DSFs, i.e. metrics that contain useful information to characterize the state of the structure, can be extracted from measured vibration time-series, possibly in near-real time, a feature which is particularly attractive for rapid loss assessment. Such DSFs can subsequently be used to construct a damage index (Farrar & Worden, 2006), whose probabilistic treatment allows to build classifiers for damage detection and localization (Abdeljaber et al., 2017; Azimi et al., 2020; Sohn et al., 2002). Such data-driven indicators can further serve as a starting point for the updating of structural models, which can be used to forecast residual capacity and remaining useful life (Limongelli et al., 2016) after the strike of an earthquake event.

In deriving data-driven indicators, Noh et al. (2011) proposed DSFs that are based on the wavelet decomposition, acknowledging the short and non-stationary nature of earthquake response signals. The time-frequency representation of wavelet decomposition is used to derive three DSFs based on the stiffness reduction that is generally linked with damage. Changes in the frequency-domain transmissibility have been shown before to indicate structural damage (Johnson & Adams, 2002). Luo et al. (2021) have proposed a DSF that compresses changes in transmissibility using a colinearity metric.

While in many applications DSFs evaluate changes in modal properties derived from ambient vibrations, potential damage that occurs during seismic events may be undetectable at low amplitudes of shaking, due to the closing of breathing cracks or the compensating effect of multiple damage sources (Astorga et al., 2018; Martakis et al., 2021a; Song et al., 2019). Thus, permanent monitoring installations are eminent for damage identification tasks, as they provide valuable information regarding the state of the structure prior, during and after seismic events.

Many vibration-based damage detection approaches have been applied and tested on slender or flexible structures, such as high-rise buildings or bridges (Gentile et al., 2016; Limongelli, 2014; Roselli et al., 2018; Solís et al., 2013; Tatsis et al., 2017). While slender structures enable the modal identification even for higher modes, which are often found to be most sensitive to damage, their dynamic characteristics do not fit the profile of stiff unreinforced masonry (URM) buildings, which present the most vulnerable elements within the European building stock. Such masonry buildings are often characterized by high lateral stiffness, local failure modes and redundancy in the lateral load-resisting system. The dynamic response of masonry buildings is often governed by a single dominant mode in each direction, posing an additional challenge to many existing approaches for damage detection. In addition, unlike steel or modern reinforced concrete structures that can be characterized as ductile, masonry buildings exhibit sudden and permanent stiffness changes, which results in a rather brittle behavior and requires DSFs that can pick up smallest changes in the dynamic behavior in short time windows.

Meaningful distribution of sensors within a building further enables localization of damaged regions of the building; when applying DSFs to subsystems of the buildings, these can offer an indication of the floor-wise distribution of damage severity, as discussed in the accompanying html file (https://yreuland.github.io/SHM_Demonstrator/SHM_Demonstration_RISE.html).

3.1 Formulation of damage-sensitive features

The following Table 1 summarizes the main features selected as part of the real-time tagging tool we develop in Task 4.4. A step-by-step description of assembly of these figures on a particular case study is offered in the accompanying html demonstrator, coded in MATLAB. The DSFs cover three approaches:

- Changes in *transmissibility*, which offers an indication of the frequency ranges, for which the signal is amplified. In buildings, peaks in transmissibility are linked to the stiffness of the structure above the reference sensor. Thus, a change in the transmissibility, detected as a loss of collinearity between a reference transmissibility and the transmissibility of the signal of a new data window, indicates stiffness reduction, as encountered during nonlinearity or residual damage. The TAC, based on the transmissibility, operates in the frequency domain.
- Changes in the *stiffness proxy*, which is obtained through numerical integration of available acceleration signals, operates in the time domain. When comparing with the KPRX from healthy reference data, this DSF provides a direct measure of stiffness loss.
- The distribution of energy in the frequency domain, obtained at discrete wavelet components, operates in the frequency domain picks up stiffness reduction through a shift of energy from the fundamental frequency towards lower frequency values. As the energy ratio is highly dependent on the ground motion, this DSF, proposed by Noh et al. (2011), has been reformulated in relative terms as the ratio between the energy spread of an output sensor and the energy spread of an input sensor.

Table 1 Summary of DSF figures adopted in the Task 4.4. formulation

DSF	Mathematical formulation	Description
Transmissibility Assurance Criterion between a sensor pair (input and output) $\boldsymbol{TAC_{io}^{m}}$ (Zhou et al., 2017)	$\mathrm{TAC}_{\mathrm{io}}^{\mathrm{m}} = \frac{\left\lvert \mathrm{T}_{\mathrm{io}}^{\mathrm{r}}\left(\underline{\omega}_{\mathrm{m}}\right)^{\mathrm{T}} \mathrm{T}_{\mathrm{io}}^{\mathrm{e}}\left(\underline{\omega}_{\mathrm{m}}\right)\right\rvert^{2}}{\left\lvert \mathrm{T}_{\mathrm{io}}^{\mathrm{r}}\left(\underline{\omega}_{\mathrm{m}}\right)^{\mathrm{T}} \mathrm{T}_{\mathrm{io}}^{\mathrm{r}}\left(\underline{\omega}_{\mathrm{m}}\right)\right\rvert \left\lvert \mathrm{T}_{\mathrm{io}}^{\mathrm{e}}\left(\underline{\omega}_{\mathrm{m}}\right)^{\mathrm{T}} \mathrm{T}_{\mathrm{io}}^{\mathrm{e}}\left(\underline{\omega}_{\mathrm{m}}\right)\right\rvert}$ is the TAC between sensors i (input) and o (output). $T_{io} = \frac{P_{oo}}{P_{ii}}$:transmissibility between $\ddot{x}_i$ and $\ddot{x}_o$; P_{xx}: spectral density amplitude of signal $\ddot{x}$;	This DSF returns the colinearity of the reference transmissibility and the transmissibility of a new - potentially damaged - data window.

	$\underline{\omega_m}$: frequency range of interest, corresponding to the m^{th} mode; r , e: reference and new state to be evaluated, respectively; $.^T$ denotes the complex conjugate of a vector.	
Stiffness proxy $\boldsymbol{KPRX_{io}^{m}}$	$$KPRX_{io}(t) = \frac{\sum_{dof=i}^{o} a_{dof}(t)}{\widehat{d_o}(t) - \widehat{d_i}(t)}$$ a_{dof}: the acceleration measured at instant t at location dof; $\widehat{d_i}$ and $\widehat{d_o}$: estimated displacement, of the input and output signal, respectively, obtained through numerical integration of the available acceleration signals.	This DSF is a direct approximator of the stiffness of the structural system.
Distribution of energy in the frequency domain $\boldsymbol{MER_{io}^{m}}$ (Noh et al., 2011)	$$MER_{io}^{m} = \frac{ME_{o,m}}{ME_{i,m}}$$ is the *relative* energy distribution between input and output, where the energy distribution, ME, is defined as: $$ME_{dof,m} = \frac{E_{dof}(\psi_m)}{\sum_{i=1}^{n} E_{dof}(\psi_{ref,i})}$$ E_{dof}: energy at discrete wavelet coefficients of a given degree of freedom, dof; ψ_m: denotes the wavelet coefficient of the m-th vibration mode; $\psi_{ref,i}$: energy at i discrete wavelet coefficients that are used as reference spread around the vibration mode, typically in the range $[0.5f_m, f_m]$, where f_m is the frequency corresponding to the m^{th} mode.	The ratio of the frequency of a fundamental mode of vibration compared with the spread of energy in the surrounding frequency bandwidth
Modal identification	Extracted by means of system identification methods (e.g. Frequency Domain Decomposition) Given the non-stationary nature of earthquake excitation, modal properties are derived from ambient vibrations not only for the reference state, but also for the potentially damaged state on the basis of post-earthquake measurements.	Modal properties, such as natural frequencies, mode shapes, mode shape curvatures, and, less frequently, damping.

3.2 Correlation of damage-sensitive features with engineering demand parameters and damage

The capacity of the selected DSFs, summarized in Table 1, to indicate the presence and scale with the extent of damage is first assessed using model simulations. In Figure 3 the relationship between the TAC (evaluated for three sensor pairs), KPRX, and MER on one hand and the average roof drift ratio (ARDR) on the other hand is shown. In addition, two IMs (PGA and the geometric mean of the spectral acceleration at 21 periods) are shown for comparison. The data is generated using a multi-degree-of-freedom model – described in Section 4.2 – for simulating the building behavior under 50 historical ground motions scaled to 14 amplitude values ranging from 0.02g to 1.4g. The results are split into two datasets, from a single parameter combination and from 20 random samples of nonlinear model parameters.

When comparing the TAC_{04}^{1} (it is recalled that the superscript 1 refers to the first mode and the subscript 04 refers to the sensor pair of input DOF 0 and output DOF 4, as defined in Table 1) with the two other TAC instances, TAC_{24}^{1} and TAC_{01}^{2}, the former, which covers the first mode of the entire structure contains less scatter and is more robust with respect to the nonlinear model parameters. The TAC and the MER are very sensitive to damage, delimitating linear from nonlinear dynamic responses. The KPRX scales with damage, even for more extensive damage levels induced by higher ARDR. While the PGA shows a very large scatter, the mean S_a is informative for lower values but present more scatter for higher values, which may not be sufficient for accurate and precise post-earthquake tagging and decision making.

These observations are confirmed by the correlation between DSFs/IMs and the maximum plastic demand (see Figure 4), which provides the maximum ratio between the maximum transient deformation and the yield deformation taken over all masonry walls. The scatter is generally higher than for the ARDR and the influence of the nonlinear model parameters is slightly more prominent.

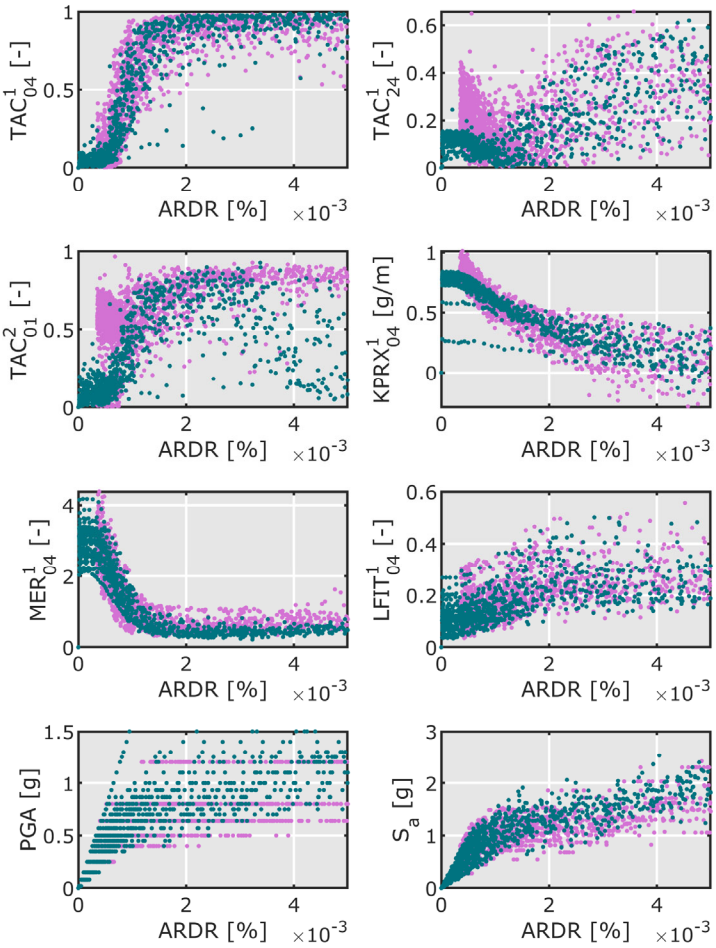

Figure 3 Relationship between DSFs/IMs and the average roof drift based on model simulations of 50 ground motions and 22 scales. The dataset is split into results from a single parameter combination (teal) and 20 random picks of nonlinear parameters, such as cohesion of masonry, compressive strength of concrete and definition of nonlinear shear springs (magenta).

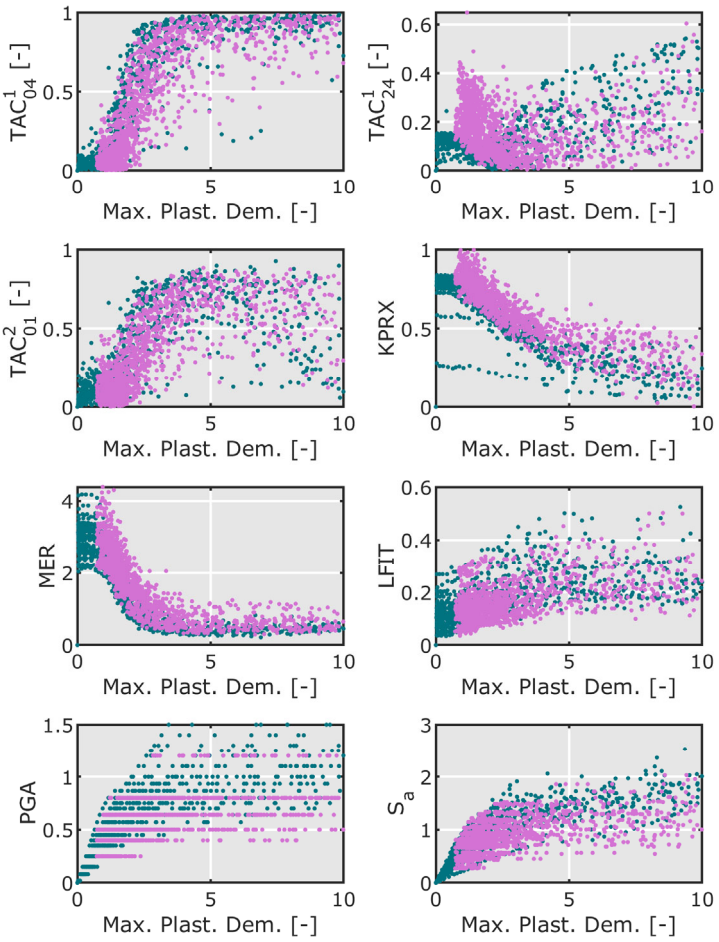

Figure 4 Relationship between DSFs/IMs and the residual stiffness reduction of masonry walls at the end of the earthquake. Results are based on model simulations of 50 ground motions and 22 scales. The dataset is split into results from a single parameter combination (teal) and 20 random picks of nonlinear parameters, such as cohesion of masonry, compressive strength of concrete and definition of nonlinear shear springs (magenta).

3.3 Robustness of damage-sensitive features with respect to sensor noise

Artificial noise is added to the model predictions to assess the robustness of DSFs with respect to noise. The evolution of the uncertainty range of derived DSFs produced by evaluating 100 random instances of artificial measurement noise is shown in Figure 5 for two earthquake instances, one resulting in linear structural response and one pushing the model in the nonlinear range.

The median of the derived DSFs is roughly stable, but the variability increases significantly when the noise level exceeds $0.05\ m/s^2$. This corresponds to high noise levels (signal-to-noise ratio of 12) and most commercially available sensors are considerably less noisy. Given that the results are still reliable, although noisy, for a noise level of $0.1\ m/s^2$, DSFs are found to be robust with respect to noise and suitable for low-cost sensing solutions – such as developed within task 2 of the RISE project.

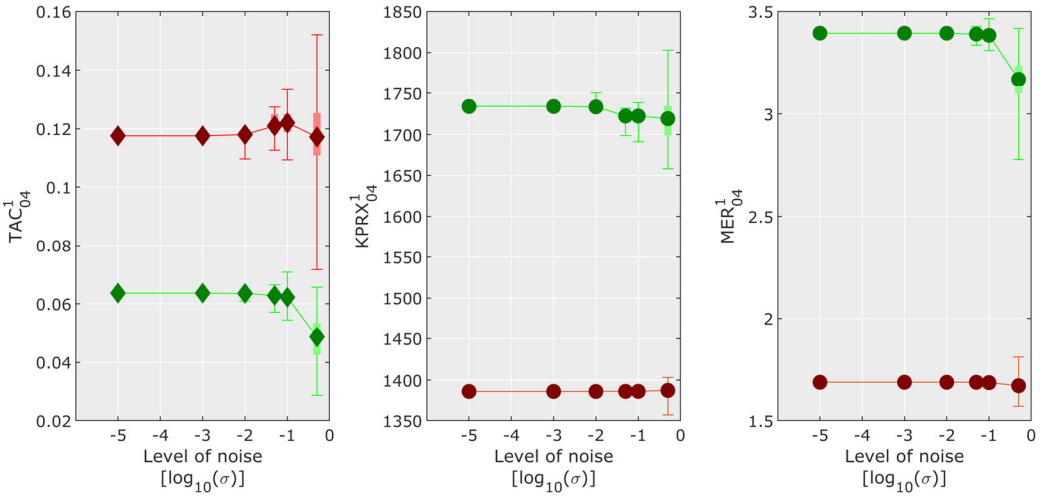

Figure 5 Sensitivity of damage-sensitive features to sensor noise (simulated as white noise with increasing standard deviation). An undamaged (green) and a damaged (red) building state are compared. Uncertainty ranges are indicated with error bars and correspond to the range of 100 noise simulations.

4. Demonstration of near-real-time building tagging

In order to illustrate and demonstrate the components of data-driven damage detection and quantification for SHM-based near-real-time tagging, a shake-table dataset is used. A MATLAB-based online tutorial on the damage-tagging is available: https://yreuland.github.io/SHM_Demonstrator/SHM_Demonstration_RISE.html.

A half-scale four-story building has been tested by Beyer et al. (2015). The tested building specimen underwent nine earthquake motions with increasing amplitude, with the last earthquake leading to collapse (unstable building) and has therefore been discarded; given SHM is not required to conclude on collapsed buildings. After each earthquake white-noise (WN) table motions have been performed and an EMS-98 damage grade (DG) has been attributed based on visual inspection of the test specimen. The main characteristics of the test runs are summarized in Table 2 and the geometry of the tested building specimen is provided in Figure 6.

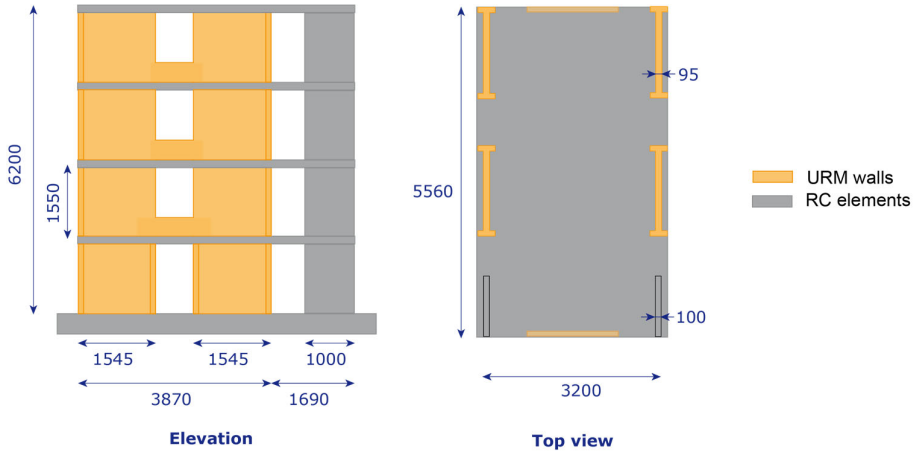

Figure 6 Geometry of the building specimen tested by Beyer et al. (2015). Figure adapted from Reuland et al. (2017).

Table 2 Description of shake-table test runs and evolution of damage in the specimen. The tests were based on scaling the ground motion measured at the Ulcinj-Hotel Albatros station during the April 15th, 1979, Montenegro earthquake. See Beyer et al. (2015) for detailed descriptions.

Earthquake #	PGA [g]	DG [EMS]	Damage description
EQK1	0.08	1	One haircrack in one wall of 1st floor
EQK2	0.13	1	Haircracks in one wall of first 2 floors and in the construction joint between wall and foundation
EQK3	0.21	1	Cracks in all masonry walls of first 2 floors
EQK4	0.35	2	Several diagonal cracks over the entire wall height of one wall of the 1st floor with negligible residual crack width. Many flexural cracks in the concrete slab of the first floor; Masonry spandrels and concrete wall remained undamaged.
EQK5	0.40	2	Same as previous.
EQK6	0.76	2	Significant increase in damage to the structure. All masonry walls with diagonal cracks at all floors. First and second floor walls present residual cracks of 0.8mm.
EQK7	0.37	2	This test, with a smaller amplitude than the previous EQK6, was intended to simulate a possible aftershock but led only to very minor additional damage to the structure.
EQK8	0.64	3	Structure was severely damaged. Damage in the masonry walls started concentrating in one diagonal crack. Diagonal cracks passed through bricks.

4.1 Detecting the presence of damage

Data-driven detection of damage requires an initial computation of the ranges that can be related to normal – or *healthy* – behaviour. Statistic damage detection methods rely on the distance between the healthy reference distribution and monitored datapoints that belong to an unknown damage class to conclude on the presence or absence of damage. When performing SHM on residential buildings, the collection of data to establish such healthy reference ranges is typically limited to ambient vibrations, which are produced by wind, micro-tremors, and human activities (e.g., traffic and construction site activity). The amplitude of ambient vibrations typically lies between $1\,\mu m/s^2$ and $1\,mm/s^2$ and the frequency content is theoretically flat (white noise), even if local soil conditions may result in non-perfect white noise (WN).

The DSFs are formulated to be independent on the frequency content and amplitude of the excitation, which enables the use of ambient vibrations to establish healthy reference ranges. However, many structures exhibit small nonlinearities in the elastic range, which does not lead to significant residual damage (see Section 5.1). This is especially true for concrete and masonry buildings, as these building materials present heterogeneities and discontinuities at the micro-scale, which leads to the opening and closure of small micro-cracks, when the amplitude of shaking increases (Martakis, Reuland, & Chatzi, 2022; Michel et al., 2011). In regions with high seismicity with frequent non-destructive earthquakes, measurement data collected under weak earthquakes that do not threaten the structural integrity would be preferred to ambient data to reduce the amplitude-dependency in the structural response.

After establishing the predominant frequency ranges and frequency spectra, the reference data is used to derive the statistical distribution of DSFs that correspond to the healthy state of the structure by splitting the healthy reference data into short time-windows. During this *training* phase, the structural state is assumed healthy. Variations in the DSFs during this *training* phase result from sensor noise, variations in the frequency content of the input motion, and environmental conditions that alter the building behavior, such as temperature and humidity. In the dataset used for demonstration, the uncertainty in DSFs arises from the first two uncertainty sources as the environmental conditions during the shake table-tests were well-controlled. To reduce temperature-dependent influences on DSFs, reference ranges can be regularly updated, for instance on an hourly basis, to reduce the difference in environmental conditions between the reference dataset and a new datapoint. An example of healthy reference distributions is shown in Fig. 7 for DSFs TAC and MER. A lognormal and normal fit are also shown in the figure and can be used to establish confidence intervals.

Based on such confidence ranges from the distribution of healthy datapoints, damage-detection thresholds can be established and may be linked with alarm messages, when consistently crossed by the measured DSFs. Given that these thresholds are purely data-driven, the link between the distance that new datapoints have from the reference distribution and the severity of damage is not yet established. Such a correlation may exist, yet multiple buildings need to be monitored to learn such correlations from monitoring data (Bodenmann et al., 2021; Goulet et al., 2015). In absence of such regional SHM implementations, a larger distance between the reference distribution and the new datapoints mostly increases the confidence in the assumption that damage is present in the structure.

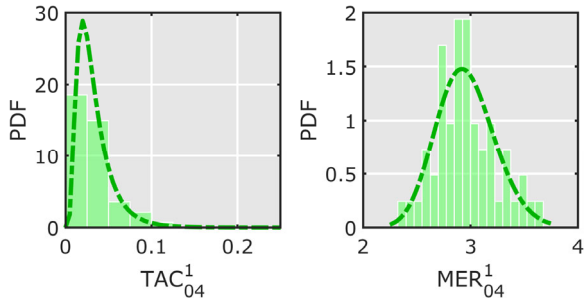

Figure 7 Reference distribution of two DSFs, TAC and MER, derived from WN excitation in healthy conditions.

Based on the healthy reference distributions, the following tags are attributed to the dots for illustration: *white* in case the datapoint falls within the 95% confidence interval; *green* if the datapoint falls within thresholds increased by 15% with respect to the 95% confidence interval; *amber* when the datapoint exceeds the thresholds increased by 15% with respect to the 95% confidence interval but remains with six standard-deviations of the healthy reference data; *red* if the datapoints falls outside six standard-deviations from the median of the healthy reference distribution.

The comparison of the DSFs during the first earthquake (dots) and the 95% confidence interval (green shaded area) of healthy reference data is shown in Figure 8 for three DSFs. While the damage sustained by the specimen was not significant, some values slightly exceed the thresholds. Several reasons can lead to such a behavior:

- While the reference values are derived for WN conditions, earthquake signals contain transient effects and do not have a stable frequency content.
- Masonry and concrete buildings are known to show a reversible amplitude-dependent stiffness reduction due to opening of micro-cracks and elastic nonlinearity (Martakis et al., 2021a).

The DSFs do not consistently exceed the confidence intervals and return within the confidence region towards the end of the earthquake, when the amplitude of shaking reduces, no damage is detected.

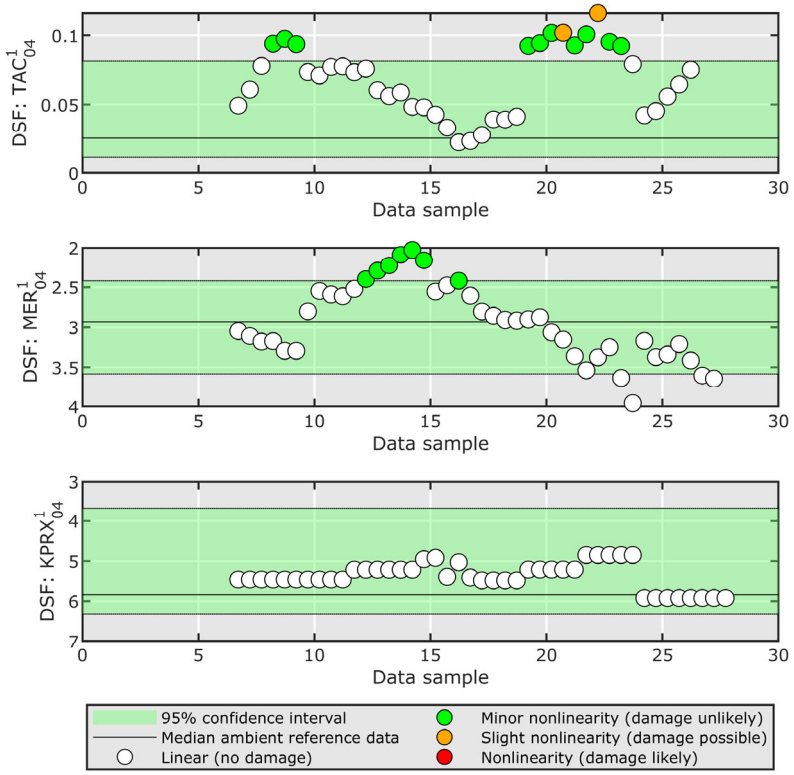

Figure 8 Comparison of three DSFs (top: TAC, middle: MER, bottom: KPRX) measured during EQK1 (see Table 1) compared with the 95%-confidence interval of healthy reference data.

The same analysis for the third earthquake signal is shown in Figure 9. The DSFs consistently exceed the healthy reference thresholds (indicated with black lines and a dark green shade) and even exceed adapted thresholds based on the first two earthquakes. Such adapted thresholds may be established when combining data-driven monitoring with visual inspections, for instance. Given the consistent exceedance of thresholds for all three DSFs, onset of damage in the structure can be confidently concluded. This observation is consistent with the observations on the specimen: despite being still classified as DG2, cracks were observed in all in-plane masonry walls of the first two floors.

Additional information on data-driven detection of damage for earthquakes EQK2, EQK5, and EQK8 can be found in the following online demonstrator: https://yreuland.github.io/SHM_Demonstrator/SHM_Demonstration_RISE.html.

The probabilistic distribution of the TAC for the fifth earthquake (EQK5) is shown in Figure 10 and the probability density function (PDF) is compared between the earthquake data and three reference datasets: the healthy reference data (Figure 10a), the WN data measured prior to EQK5 (Figure 10b), and the earthquake data from the preceding EQK4 (Figure 10c). While damage is present in the structure (with respect to the healthy condition), no significant increase in damage is observed with respect to the previous earthquake EQK4, neither with respect to the earthquake signal itself nor with the WN data measured prior to EQK5. This capacity of statistical damage detection to keep track of both, the absolute damage and the increase in damage, is of interest for damage accumulation in buildings during earthquake sequences and thus, enables time-dependent damage characterization.

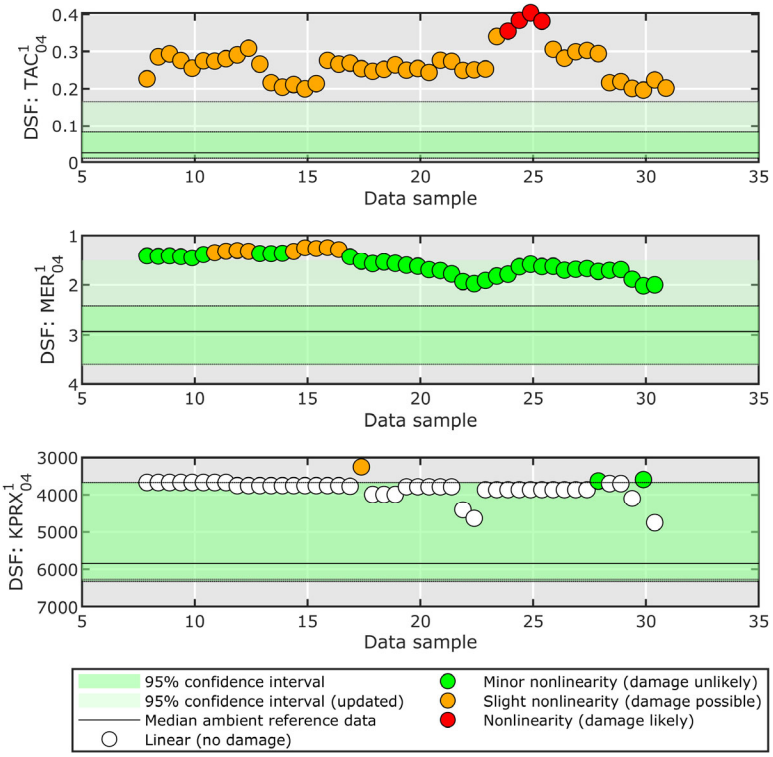

Figure 9 Comparison of DSFs (top: TAC, middle: MER, bottom: KPRX) measured during EQK3 (see Table 2) with the 95%-confidence interval of healthy reference data and an extended confidence interval (shown in light green) based on the data from the first two earthquakes.

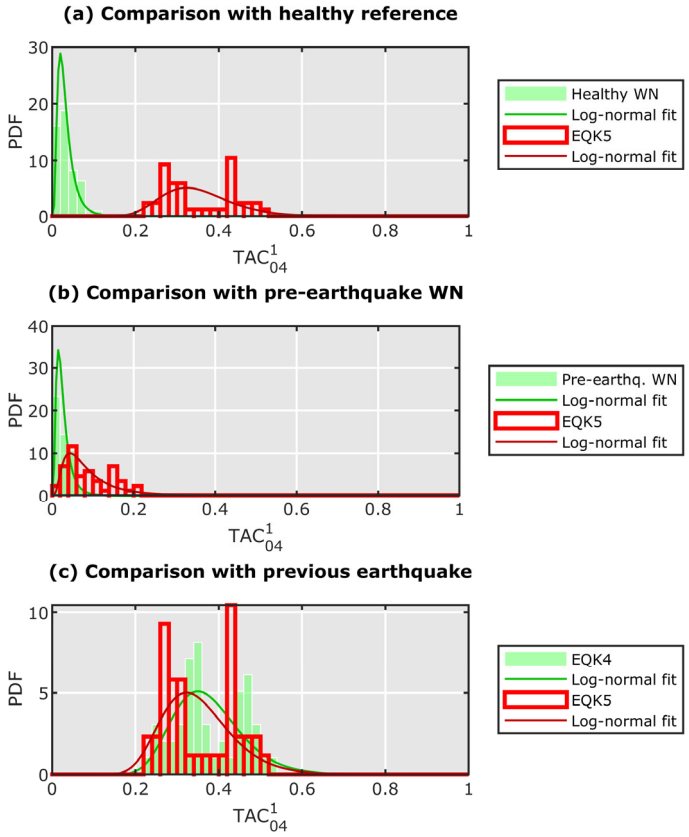

Figure 10 Probabilistic evaluation of the TAC, computed for short and overlapping time windows. The PDF of the TAC is measured during EQK5 is compared with: (a) the healthy reference WN signal, (b) the WN signal measured between EQK4 and EQK5, and (c) the TAC measured during EQK4. While the building is damaged during earthquake 5 (as can be seen in subplot a), little additional damage with respect to the previous earthquake is sustained by the structure. This underlines the capacity of DSFs to track the evolution of damage over time, for instance during earthquake sequences.

The PDF of the TAC during EQK6 is shown in Figure 11. Unlike for EQK5, this earthquake introduced significant damage into the structure. This increase to the damage is not only detected by the higher values of the TAC with respect to the healthy reference signal (Figure 11c) when compared with EQK5 (Figure 10a) but also by the strong divergence with the pre-earthquake WN signals (Figure 11b), which are representative of the damage-state prior the EQK6.

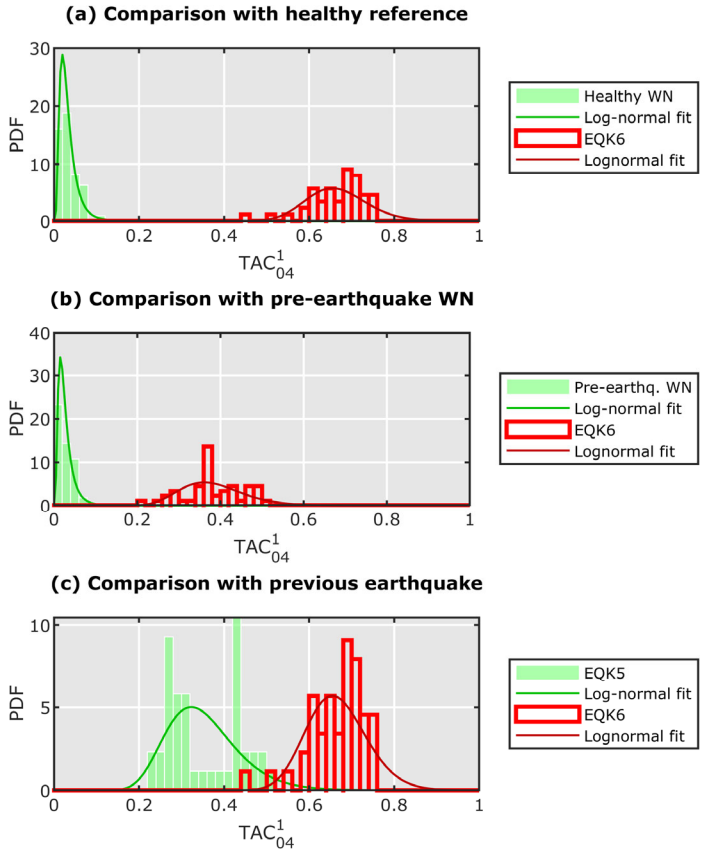

Figure 11 Probabilistic evaluation of the TAC, computed for short and overlapping time windows. The PDF of the TAC is measured during EQK6 is compared with: (a) the healthy reference WN signal, (b) the WN signal measured between EQK5 and EQK6, and (c) the TAC measured during EQK5. Unlike for EQK5, shown in Figure 10, the structure sustains significant additional damage during EQK6. This is evidenced by the shift to higher TAC values, with respect to the pre-earthquake WN (a) and the previous earthquake EQK5 (b).

A quantitative comparison of PDFs can be achieved using the Kullback-Leibler (KL) divergence (Kullback & Leibler, 1951), Div_{KL}, which is a metric of the distance between two distributions, derived using Eq. 1:

$$Div_{KL}(f) = \sum_x f^r(x) log\left(\frac{f^r(x)}{f^e(x)}\right) \quad (1),$$

where f is a PDF evaluated at values x and the superscripts e and r denote the earthquake and the reference distributions, respectively.

When applied to the two earthquake signals EQK5 and EQK6, the KL divergence values underline the observations made in Figure 10 and Figure 11. While some damage is present in the structure during EQK5, this damage has been sustained before and little additional damage is observed. Conversely, the specimen contains more damage during EQK6, which also represents a significant increase in damage with respect to the previous earthquake and the pre-earthquake WN signal.

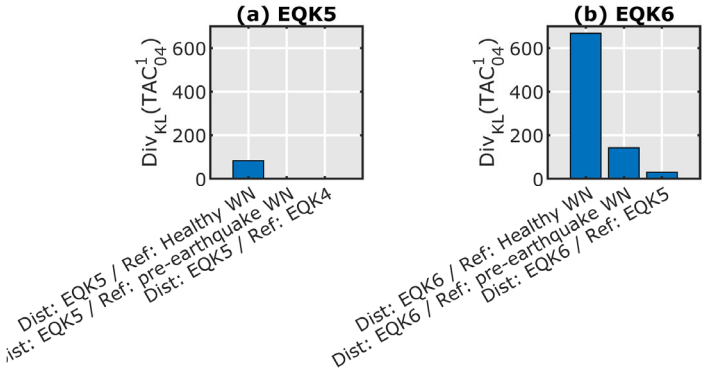

Figure 12 The absolute and cumulative tracking of damage can be summarized by the KL divergence between the distribution of the TAC from an earthquake and changing reference distributions. This is underlined by comparing the KL divergence for the TAC of EQK5 (a), during which little additional damage is sustained, with the KL divergence of the TAC of EQK6 (b), during which significant additional damage is sustained.

An additional demonstration of the capacity of the TAC to track the evolution of damage is shown in Figure 13, which contains a representation of the TAC over time including all 8 tested earthquakes. As can be seen, damage exists but remains very low for the first 2 earthquakes. The damage increases progressively during EQK3 and EQK4, before the structural condition drastically deteriorates during EQK6. The fifth earthquake (EQK5) and the seventh earthquake (EQK7), which has a lower amplitude than the previous earthquake, do not introduce significant damage into the structure. Despite not enabling a straightforward quantification of damage, this data-driven indicator further delivers information on damage severity, with respect to known previous structural state.

Although the healthy reference is established on ambient vibrations, the DSFs are derived from earthquake signals. This choice stems from the fact that during strong motions, the nonlinearity sustained by the structure is larger, while the structure regains stiffness during post-earthquake ambient vibrations (Astorga et al., 2018). However, given amplitude-dependent effects (see Section 5.1), transient signals, and the frequency content of the earthquake signal may influence the DSFs, a comparison with the TAC derived for post-earthquake WN is provided in Figure 14. While the trend is the same than for the TAC derived from earthquake signals, the sensitivity achieved with WN-based DSFs with respect to damage is reduced. This is in agreement with the theory, as the residual stiffness drop is less significant than the minimum transient stiffness during an earthquake event and justifies the choice of earthquake signals for damage detection.

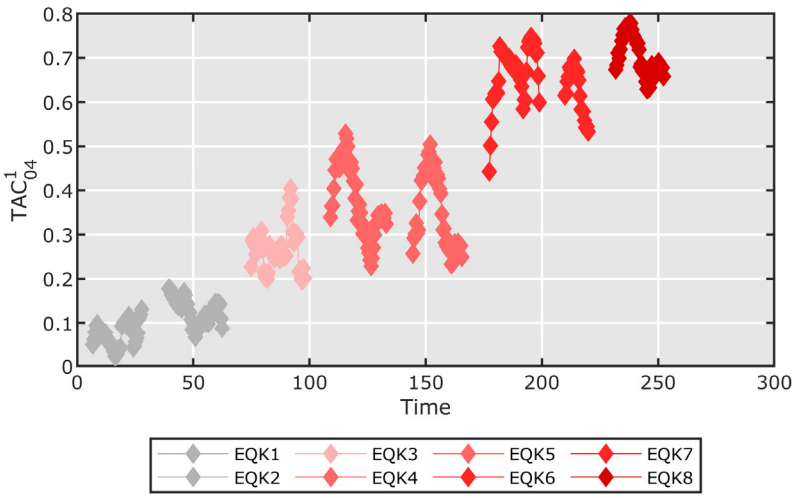

Figure 13 Evolution of the TAC over the eight earthquakes, when damage in the structure increases gradually. A significant increase is observed for EQK3, EQK4, EQK6, and EQK8, which correspond to earthquakes that increase the structural damage significantly.

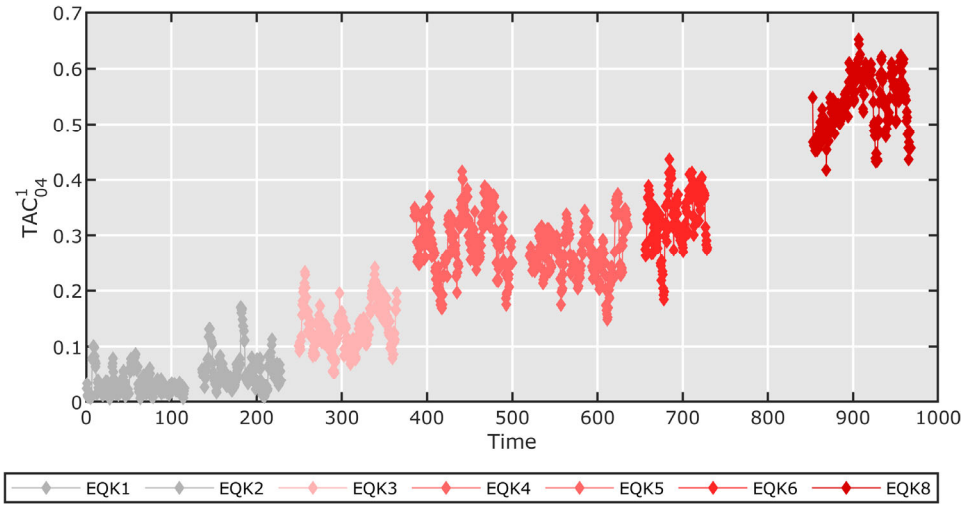

Figure 14 Evolution of the TAC derived from post-earthquake WN over the eight earthquakes (no WN test was conducted after EQK7), when damage in the structure increases gradually. A significant increase is observed for EQK3, EQK4, and EQK8, which correspond to earthquakes that increase the structural damage significantly. However, the sensitivity of the TAC with respect to damage is less pronounced when it is derived from WN than when it is derived from the earthquake signal (see Figure 13).

4.2 From features to damage tags: the role of physics-based models

While purely data-driven models are adept at the task of damage detection, and possibly its localization, building tagging implicitly involves damage quantification, with the purpose of characterizing the induced faults and to offer hints for assessment of residual capacity. These higher complexity tasks in terms of damage identification and characterization require finer grain information, which can be furnished via use of physics-based (engineering) models.

Nonlinear building models

Structures that experience seismic shaking are shifted to a nonlinear response regime. This implies that any considered structural model should account for the inherent material and geometric nonlinearities as well as the dynamic and hysteretic effects that describe such systems. While regional applications often rely on single-degree-of-freedom models (Martins & Silva, 2021; Orlacchio et al., 2021; Villar-Vega et al., 2017), we implemented a multiple-degree of freedom mode, to reduce the discrepancy between sensor data and model predictions.

The tested specimen is a mixed building with reinforced-concrete (RC) shear walls and URM walls, therefore a coupled model combining a shear-dominated part modelling the URM walls and a bending-dominated part modelling the RC shear wall is used (see Figure 15). The shear-dominated part and the bending-dominated part are connected using truss elements, as typically done for high-rise buildings (Capsoni & Moghadasi Faridani, 2016).

The OpenSees software framework (McKenna et al., 2010) is used to implement the modelling strategy. The nonlinearity of the URM walls is lumped into shear springs, modelled as *pinching4* springs (Mazzoni et al., 2006). The RC shear wall is modelled as a beam element with the nonlinear *Concrete02* material.

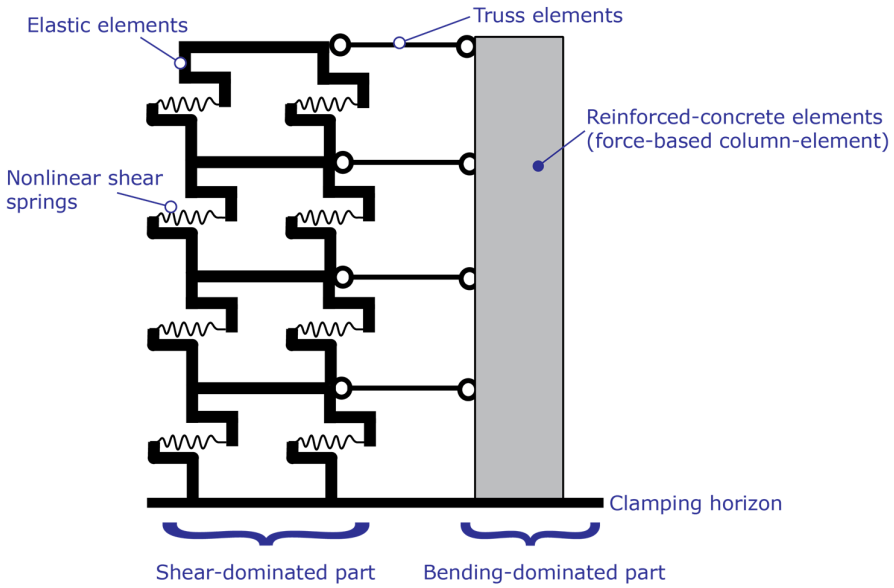

Figure 15 Multi-degree of freedom model for simulation of nonlinear behavior under earthquake loading of the building specimen that has been tested on a shake table.

The construction of fragility curves requires multiple forward dynamic simulations of the building model. Therefore, 50 ground-motion signals have been scaled to 14 amplitude values ranging from 0.02g to 1.4g.

An important step in constructing fragility curves consists in defining damage states. While presenting a crucial step, a universal definition is not available. The following damage-state attribution has been adopted:

- *Slight damage* – corresponding to a green tag – is attributed to the structure, if less than four wall elements yielded
- *Moderate damage* – corresponding to an amber tag – is reached, when more than four wall elements yield, if any URM spring exceeded a drift corresponding to 2.5 times the spring's yield drift. In addition, moderate damage is reached when the average roof drift ratio (ARDR) exceeds 1.5 times the ARDR corresponding to the yield point, derived with a static nonlinear (pushover) analysis, a value often adopted for URM buildings (Lagomarsino & Giovinazzi, 2006).
- *Extensive damage* – corresponding to a red tag – is attributed to the simulation runs, for which the ARDR exceeded 40% of the estimated maximum ARDR, corresponding to a drift of 0.4% - often attributed to the ultimate shear deformation of URM.

While this damage-state attribution presents only one option among many, the framework is flexible with respect to the exact formulation and the number of damage states, which could be elaborated together with decision-makers.

Fragility curves are derived by least-square optimization of a log-normal cumulative density function, formulated as $p(d \geq D_i|x) = 0.5 \cdot (1 + \mathrm{erf}(\log(x) - a)/b)$, where D_i denotes damage state i; x corresponds to either an IM characterizing the ground motion or a measurable DSF; a and b denote two variables to be derived through optimization; and $erf(x)$ denotes the error function that gives the probability of a random normally-distributed variable falling in the range $[-x, x]$, given by $erf(x) = \frac{2}{\sqrt{\pi}} \int_0^x e^{-t^2} dt$.

A classical fragility curve is derived with respect to an advanced IM (the geometric mean of spectral acceleration values at 23 periods) that characterizes the ground motion. This fragility curve is shown in Figure 16. The fitted curve is shown as a dotted line along the cumulative distribution of the simulation results.

As explained in Section 2.1, reformulating fragility functions with respect to measurable DSFs is proposed. Such DSFs include the building response during the earthquake, which is expected to reduce uncertainties in the post-earthquake building tagging. In order to reduce the influence of the properties of ground-motions signals, such as earthquake duration and distribution of energy over time, the fragility functions are formulated with respect to median values of DSFs over the duration of an earthquake. This approach presents a loss of information with respect to the time-evolution of DSFs, as shown for example in Figure 8 and the probabilistic distribution of DSFs, such as shown in Figure 10. Therefore, a combination of statistical damage-detection and model-based damage quantification may offer additional robustness.

Such fragility curves are shown in Figure 17 for the TAC, Figure 18 for the KPRX, and in Figure 19 for the MER. For the TAC and the KPRX, a good separation between the damage-states is observed. The MER separates green tags from damaged buildings, which is of high importance, but does not provide a high performance in delimiting amber and red tags.

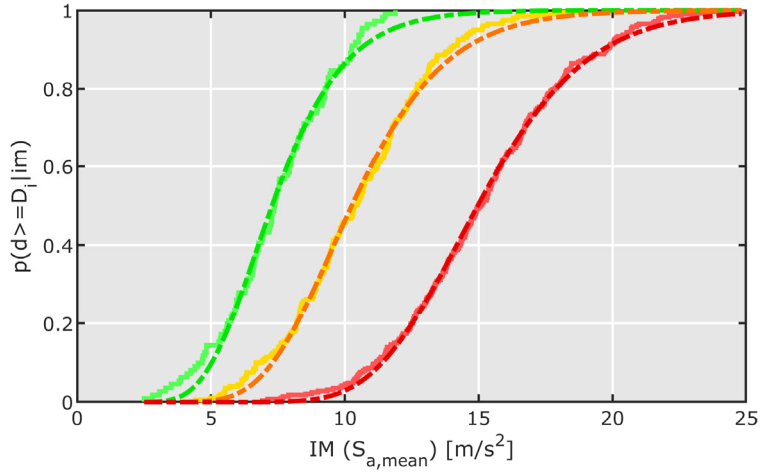

Figure 16 Classical fragility function with respect to an IM that characterizes the ground motion.

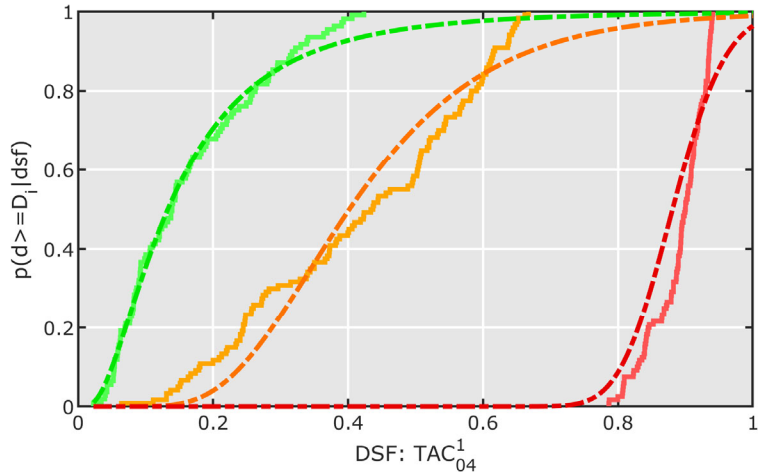

Figure 17 Fragility function with respect to the TAC, a DSF that can be measured within the structure.

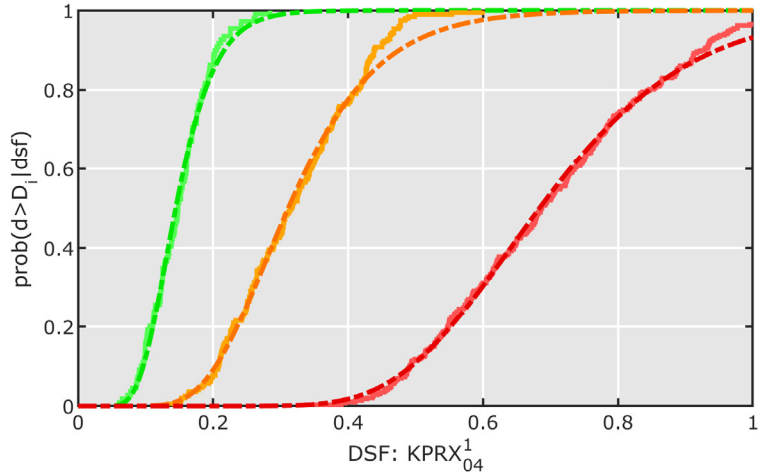

Figure 18 Fragility function with respect to the KPRX, a DSF that can be measured within the structure.

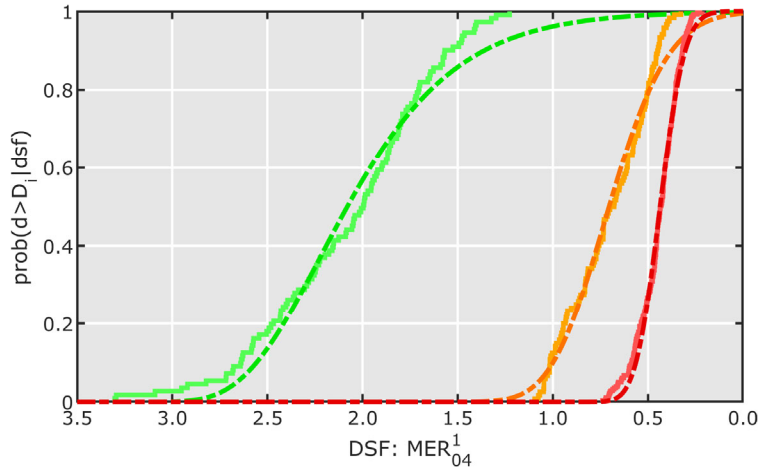

Figure 19 Fragility function with respect to the MER, a DSF that can be measured within the structure.

4.3 Application to shake-table test data

As described in the previous Section 4.2, DSF-based fragility functions need to be formulated with respect to median DSF values, in order to increase their robustness with respect to variations of the ground-motion. The correlation of the median TAC with four metrics of nonlinearity/damage – namely the hysteretic work, the DG (EMS-98 damage scale) observed from visual inspection on the specimen after the test, the peak transient roof drift ratio, and the residual roof drift ratio – is shown in Figure 20. In a similar manner, the correlation between a second DSF (MER) and the four nonlinearity indicators is provided (see Figure 21).

The following observations are made:

- As for the model predictions, the nonlinearity indicators scale well with the DSFs.
- While the DSFs do not provide a strong deviation between the strong earthquakes (EQK6 and EQK8), they provide a clear separation between non-damaging earthquake (EQK1 & EQK2) and damaging earthquakes, as well as between slight and extensive damage. This is a necessary starting point for successful building tagging based on a traffic-light logic.
- When compared to visually observed DGs (EMS98 damage scale), the DSFs provide a more refined estimation of damage, which could be of interest for subsequent repair design (as made in RISE task 4.3).
- Figures 19 and 20 are established with respect to the healthy reference state. A more refined increase in damage for the strong earthquakes EQK6 and EQK8 may be obtained by redefining the reference (as shown in Figure 11), thus paving the way towards state-dependent damage detection (i.e. assessing the increase in damage, rather than the presence of damage).

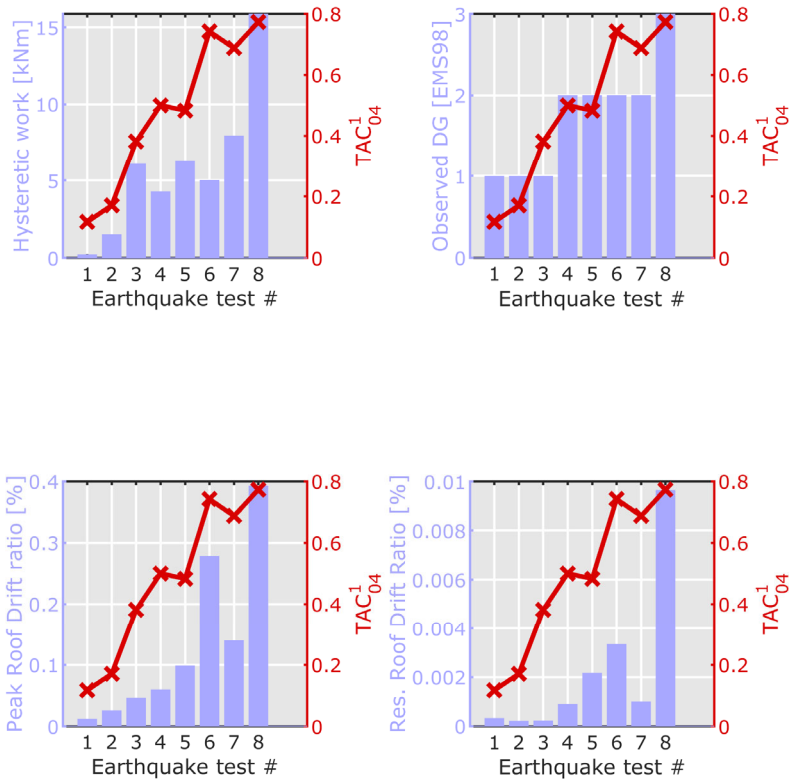

Figure 20 Correlation of the TAC with four nonlinearity indicators: hysteretic work (top left), damage grade (DG) observed from visual inspection after the test (top right), maximum transient roof drift ratio (bottom left), and residual roof drift ratio (bottom right).

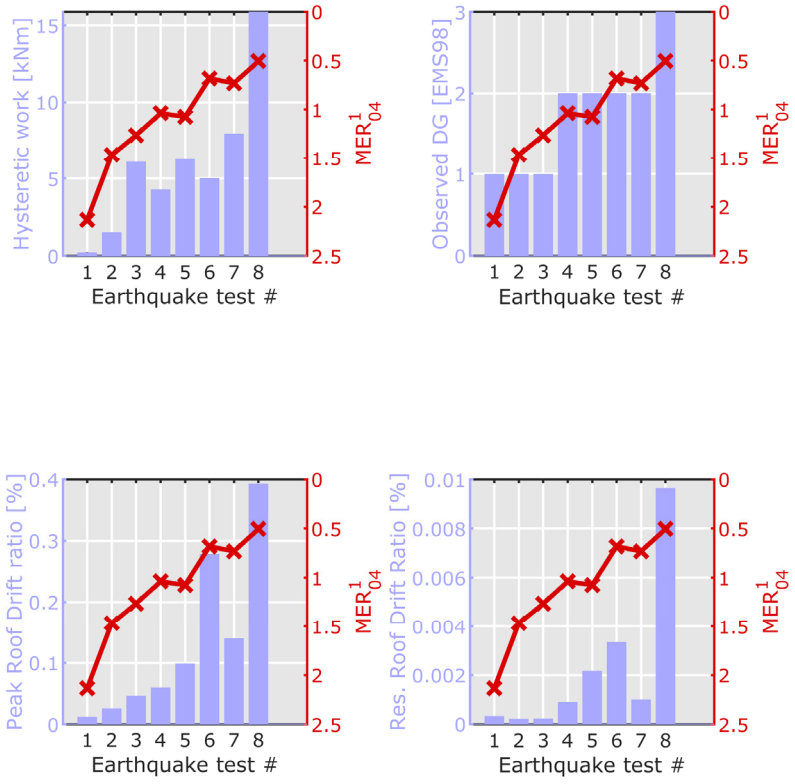

Figure 21 Correlation of MER with four nonlinearity indicators: hysteretic work (top left), damage grade (DG) observed from visual inspection after the test (top right), maximum transient roof drift ratio (bottom left), and residual roof drift ratio (bottom right).

The combination of the TAC values, derived from measured acceleration and shown in Figure 20, and the DSF-based fragility functions (plotted in Figure 17) lead to a prediction of the probability of the building exceeding a given damage-state, analogously to damage-state predictions with classical fragility curves. The predicted probabilities – which sum up to 1 – are shown for all eight earthquake signals in Figure 22. The white bar consists in a fully linear structure that did not even sustain minor damage (see Section 4.2 for the definition of damage states). Based on the TAC, the building is not predicted to sustain extensive damage, not even under EQK8. This is a result of the high median TAC value for extensive damage by the physics-based model and shows some limitations of model predictions with respect to real dynamic hysteretic behavior of buildings. Nonetheless, post-earthquake inspection of the building after EQK concluded in DG3, which does not necessarily correspond to extensive – but rather moderate – damage, meaning that observations and predictions are in correspondence.

The damage tags predicted with the MER-based fragility function are shown in Figure 23. Compared against the TAC-based predictions, the results are slightly less conservative and predict green tags with more probability. On the other hand, the KPRX-based predictions (see Figure 24) tends towards more conservative predictions, especially for the stronger earthquakes. Again, these discrepancies show the limit of simplified model to predict dynamic nonlinear behavior of structures.

To reduce the dependency on a single DSF, the predictions from all three DSFs are combined into a single probabilistic prediction, as shown in Figure 25. Importantly, combining several DSFs does not incur additional costs or model simulations, but rather extracts more information from the same signals, whether measured or simulated.

A building tag is attributed based on the following logic:

- If the joint probability of no and minor damage exceeds 80% or if $Centroid_{DS}$ is below 1.33, then a green tag is issued. The $Centroid_{DS}$ is derived as:
  $Centroid_{DS} = p(d \geq 'None') \cdot 0 + p(d \geq 'Minor') \cdot 1 + p(d \geq 'Slight') \cdot 2 + p(d \geq 'Extensive') \cdot 3$.
- If the joint probability of slight and extensive damage exceeds 60% or if the probability of extensive damage exceeds 25%, a red tag is issued. This is a conservative approach that yields a rather high probability of red tags, owing to the reduced seismic capacity of damaged buildings.
- An amber tag is issued for buildings that have neither a green nor an amber tag.

The exact logic for attribution of tags influences the number of green, amber, and red tags and thus, the number of evacuated people. Therefore, such tagging rules should be established together with competent authorities, such as civil protection.

The tags that are attributed to the test building are shown in Figure 25 as the background color of the probability plots. In general, the tags are reasonable given the observations made on the building specimen (see Table 2). Less conservative attribution rules – for instance based on the tag with the highest probability – would have resulted in a green tag after EQK5 and an amber tag after EQK8 – which is even more in line with the attributed damage grades from visual inspection.

In addition, if the building is tagged safe after EQK4, the purely data-driven approach, outlined in Section 4.1, would have led to the conclusion that little additional damage is present in the structure after EQK5. Such a combination of data-driven and model-based tagging is a promising future development of seismic SHM.

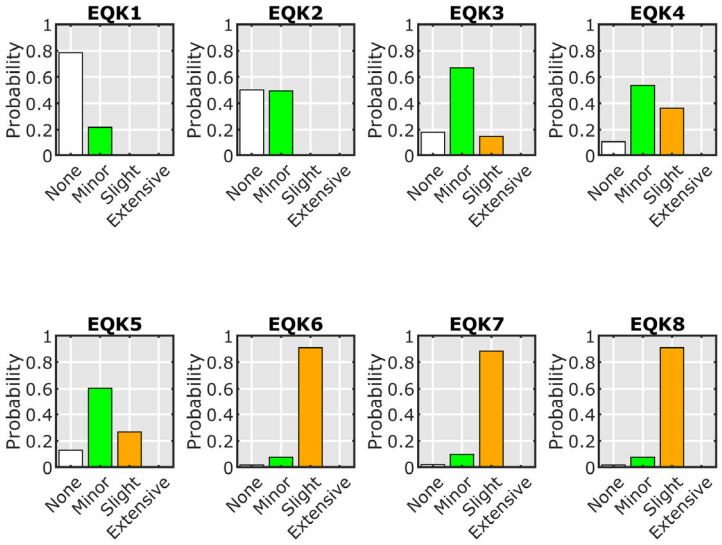

Figure 22 Prediction of post-earthquake building tag probabilities based on TAC for all eight ground motions.

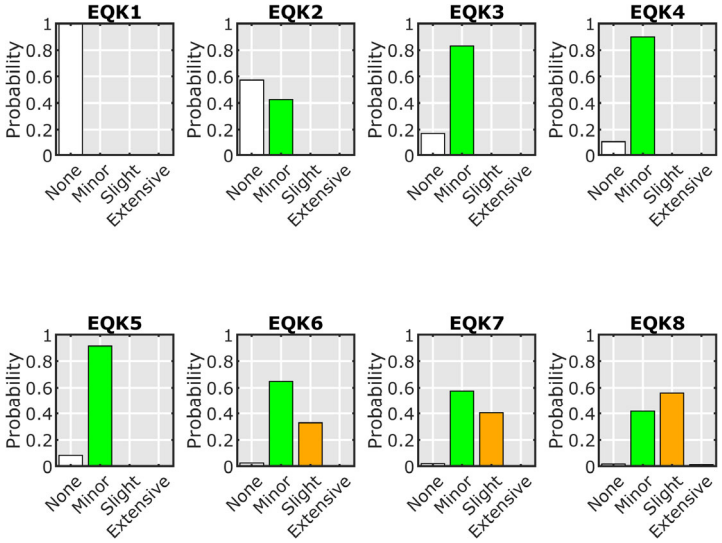

Figure 23 Prediction of post-earthquake building tag probabilities based on MER for all eight ground motions.

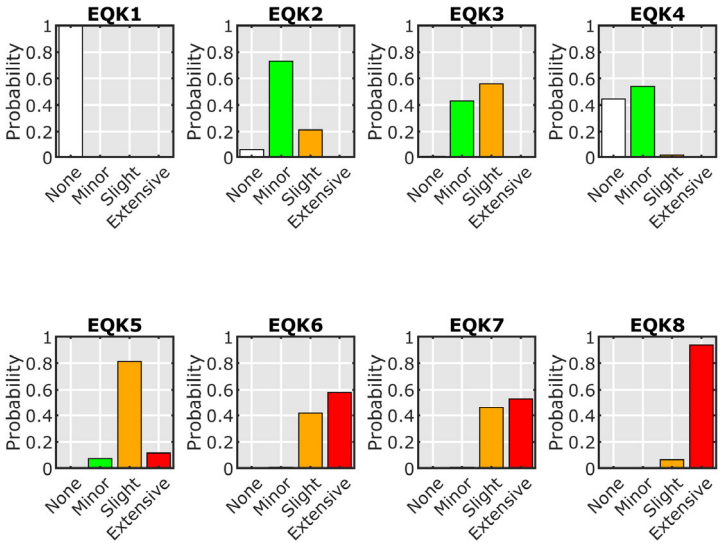

Figure 24 Prediction of post-earthquake building tag probabilities based on KPRX for all eight ground motions.

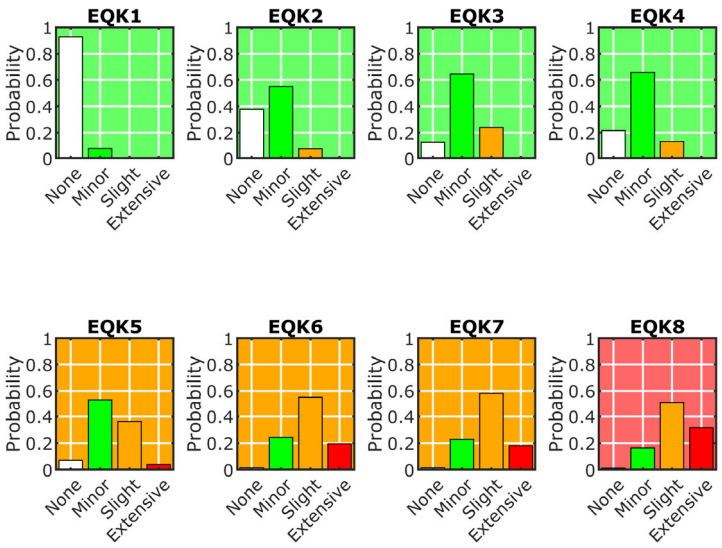

Figure 25 Prediction of post-earthquake building tag probabilities for all eight ground motions based on the combination of the three DSFs: TAC, MER, and KPRX. The final tag, attributed based on tagging criteria, corresponds to the background color of the subplots. The probability of extensive damage remains low, yet arises from EQK, which corresponds to the first earthquake, for which major damage has been observed on the specimen.

5. Perspectives on data-driven building tagging

5.1 Quantifying undamaged amplitude-dependent stiffness changes by monitoring demolitions

Ambient vibration measurements offer reference measurements to establish the healthy ranges and dynamic properties of existing buildings. Yet, the comparison of ambient and forced vibration experiments in real scale structures has brought to light the existence of reversible nonlinear behavior due to changes in excitation amplitude. (Song et al., 2019) investigated the inferred stiffness properties of a two-storey concrete building for varying excitation amplitude and observed an almost linear decreasing relation between the identified frequencies and the excitation amplitude. (Michel et al., 2011) used a shaking mass to study the amplitude-dependent modal properties and proposed a link between natural frequencies from ambient vibrations and an equivalent elastic stiffness.

In order to increase the dataset of amplitude-dependent dynamic properties of existing URM buildings in Europe, we conducted vibration monitoring of multiple buildings during their planned demolition in the greater Zurich area in Switzerland (Martakis, Reuland, & Chatzi, 2022). The acceleration data recorded during construction-site activities, prior to the first damage to structural elements, allows for extraction of signal windows exhibiting changing levels of shaking, while ensuring that the findings are not influenced by any damage. In regions with low-to-moderate seismic hazard, such as Switzerland, measurements during demolition activities form a valuable – if not exclusive – source of vibrations to study the amplitude-dependency in the response of masonry building to dynamic loadings. Eventually, such data contributes to formulate robust thresholds for normal behavior of masonry structures in view of data-driven damage-detection schemes, such as described in the previous sections.

Monitoring planned demolitions

In the following, the results for three measured real-world buildings, also presented in the RISE deliverable MS37, are briefly presented. By means of the Stochastic Subspace Identification algorithm (van Overschee & de Moor, 1996), a baseline estimation of the modal properties is established (see

Table 3). The demolition of masonry buildings involves gradual removal of elements, typically from the top to the bottom of the building, with the shovel of an excavator (see Figure 26). Most of the non-structural elements are removed beforehand, leaving the structure at a bare state. During demolition, buildings are subjected to hits and pulls of arbitrary direction and intensity. Such impulse-like hits provide a rich variety of dynamic building responses. As the demolition starts from the roof, there is time window without removal of substantial mass or damage to structural components.

With the Eigensystem Realization algorithm (ERA) (Juang & Pappa, 1985) the modal properties of the building are derived for the time-windows of each individual impulse. Details on the derivation of modal properties under impulse responses recorded during demolition can be found in (Martakis et al., 2021a).

Characteristic impulse responses of different amplitude levels are plotted in Figure 26 (right). The corresponding displacements are approximated for illustration through double integration of the acceleration signals. The maximum computed displacement is below $0.05\,mm$ and the equivalent linear range is typically considered to extend until 1 mm (Lagomarsino & Cattari, 2015; Martakis et al., 2021a). Thus, the structure is assumed to respond in the elastic range during demolition and no damage due to excessive loading is expected. In addition, the transitory nature of the stiffness drop is verified, as there is no trend towards reduced frequencies over time.

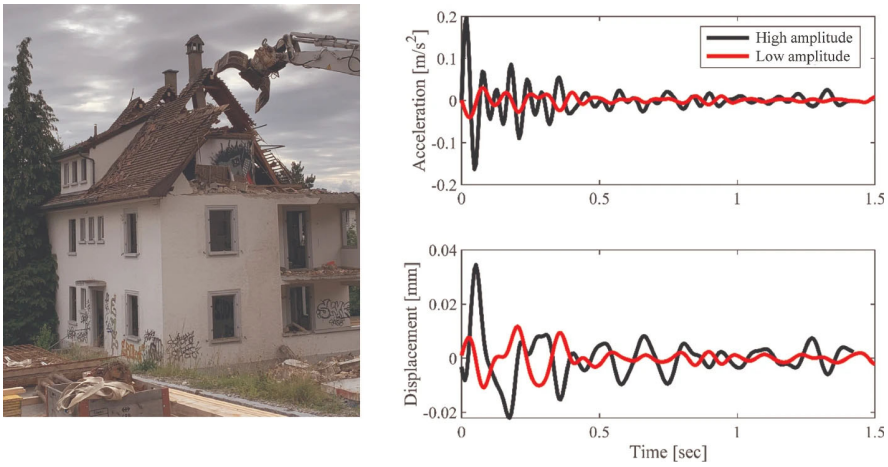

Figure 26 Demolition process from top to bottom with an excavator shovel (left) and characteristic impulse responses of various amplitude levels (right).

All three measured buildings are URM buildings and have been built in the first half of the 20th century, before the introduction of seismic prescriptions into Swiss building codes. Such masonry buildings, lacking seismic design, form the largest part of the Swiss building inventory. Photos of the buildings prior to the start of the demolition are provided in Figure 27. All three buildings have a residential function and consist of two regular floors above ground level, in addition to an attic in the steeply sloped roof, and one floor, which is either partially or fully placed under the ground level. A detailed description of the building properties, following the Global Earthquake Model taxonomy (Crowley et al., 2012), is reported in

Table 3. All three buildings are mostly regular in plan and elevation. The dynamic response of buildings to hits with the excavator are recorded using eight tri-axial MEMS-based accelerometers, which are distributed over the height of the building at strategic locations at the slab levels of the buildings, as shown in Figure 27.

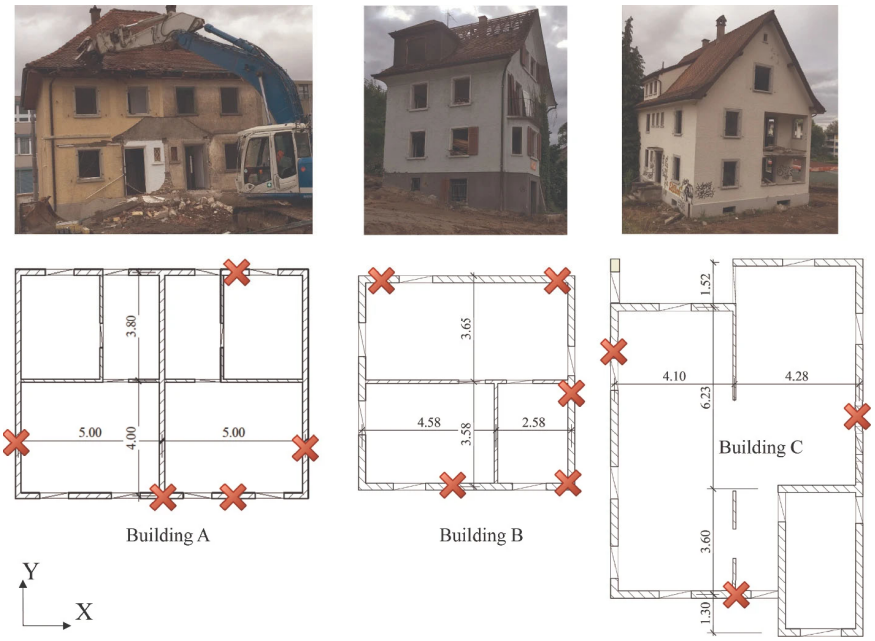

Figure 27 Photos of the three buildings taken prior to the demolition (top) and floor plans of the three studied URM buildings with sensor positions are marked with red crosses (bottom). Additional details of the measurements can be found in RISE milestone 37.

Table 3 Properties of the studied buildings.

Property	**Building A**	**Building B**	**Building C**
Year of construction	1922	1927	1930
Number of floors (above ground)	2 + Attic	2 + Attic	2 + Attic
Number of floors (below ground)	1	1 (partially below ground)	1 (RC, partially below ground)
Floor system	Flexible wooden floors	Flexible wooden floors	RC floor (cast-in-place)
Roof system	Sloped, flexible wooden rafters	Sloped, flexible wooden rafters	Sloped, flexible wooden rafters
Occupancy	Residential	Residential	Residential
Footprint	78 m^2	52 m^2	94 m^2
Natural frequency (from measurements)	6.4 Hz (bending X) 7.4 Hz (bending Y)	6.9 Hz (bending X) 5.8 Hz (bending Y)	6.0 Hz (bending X) 7.3 Hz (bending Y)

Amplitude-dependent reduction of natural frequencies

Construction activities with heavy machinery prior to the actual demolition (removal of non-structural elements, site-preparation works etc.) generate a large dataset of hits that cover a multiple amplitudes, directions, and durations. Using the ERA algorithm, which is particularly suited for analysis of impulse response signals, the dynamic properties are derived for each hit. The frequency corresponding to the first bending mode in the direction with the strongest hits is shown for all three buildings in Figure 28. The frequencies are normalized with respect to the corresponding reference frequency obtained before demolition activities started (see

Table 3). Although input excitations cannot be measured directly, the intensity metrics of the building response serve as a proxy to cluster the impulses into groups of similar amplitude. The maximum root mean square (RMS) acceleration among all sensors is chosen here as such an intensity metric.

A clear frequency drop with increasing amplitudes can be observed for all three URM buildings. For building A, more hits have been recorded and the increased number of hits in the low-amplitude range (below 1 mg) translates to a higher variability. Thus, for building A, the identified

frequency follows an almost normal distribution with a mean of 0.98 and a standard deviation of 0.03, both with respect to the reference frequency derived from ambient vibrations.

A comparison of the frequency distributions obtained for impulses with low and high RMS, respectively, shows the reduction of frequency. However, the drop is larger for buildings A and B, with a mean around 10% frequency drop, while building C shows less than 5% frequency drop, even if the hits have similar intensity. The structural system – building C, unlike buildings A and B, has stiff RC floors – may explain the lesser amplitude-dependency of the frequency. For building A, on the other hand, the stiffness reduction is notable for hits with the RMS of acceleration (a_{RMS}) exceeding 2, this tendency starts at lower intensity for building B (at $a_{RMS} = 1mg$) and building C (at $a_{RMS} = 0.7mg$). As the acceleration may depend strongly on the location, angle, direction and severity of the hit with the shovel, as well as the distance between the hit and the closest sensor, approximate drift values are recommended to be used in future work to yield more stable results. However, deriving approximate displacements, requires accelerometers with high sensitivity and no drift in low frequencies. Still, the amplitude, at which the stiffness starts to drop significantly, and the level of drop may be building-dependent. While the intensity measure is chosen to be the maximum RMS acceleration of all channels, other measures, such as Arias intensity and peak acceleration have also been assessed, showing a lesser fit.

Nonetheless, the observed drop of the stiffness of the structural system, when vibrations exceed amplitudes that are typically associated with ambient conditions, is valuable as it lays the foundation for several applications of SHM in seismic context:

- formulating correlations between properties derived from ambient vibrations and properties under large-amplitude shaking is crucial for predictions of nonlinear behavior and the ultimate capacity with models, whose elastic properties are updated using vibration measurements (Martakis, Reuland, Imesch, et al., 2022).
- data measured in full-scale systems help in attributing the source of nonlinearity to possible sources, such as soil-structure interaction, masonry stiffness and transfer of forces between structural elements (Martakis et al., 2021b).
- deeper understanding of the reversible amplitude-dependent variations of modal properties is required to reduce the probability of false positives in automated data-driven damage-detection setups, as proposed in Section 2 and demonstrated in Section 4.

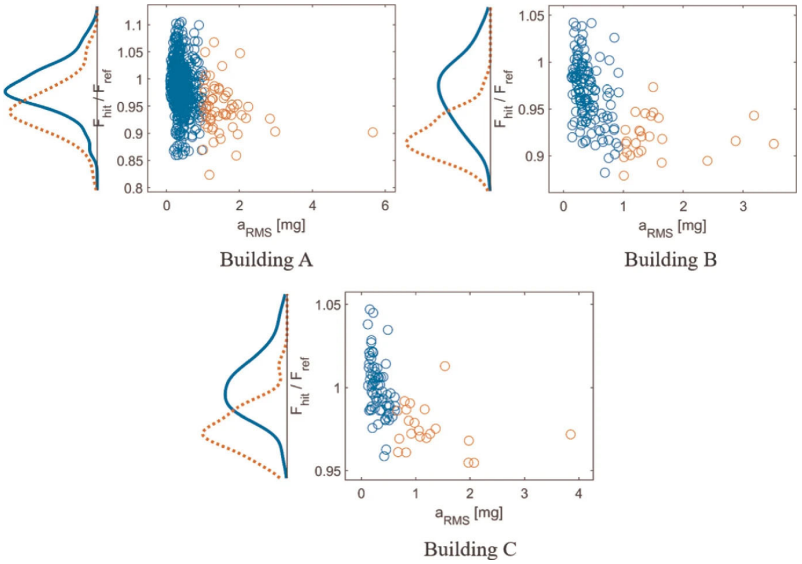

Figure 28 Frequencies, derived with the ERA from the hits measured in three buildings. Frequencies correspond to the mode in the direction of the strongest hits and are normalized with respect to the reference identification under ambient vibrations. For better readability, axis differ between the three subplots.

5.2 Domain-adaptation from model to shake-table tests

A known bottleneck when training methods that rely on monitoring data that are specifically extracted from a small subset of instrumented structures is their ability to generalize in terms of condition assessment of further building structures. As part of the tools developed in Task 4.4 of RISE, we demonstrate a domain adaptation scheme that boosts generalization potential. As an operation, domain adaptation aims to improve the predictive performance of a classifier in the target domain, for which no labels are available, by training the classifier with labelled data from a source domain (where data is richer) and limited unlabeled data from the target domain. In this case, the source domain consists of a simulation model (Figure 29), which is a parametrized two-dimensional equivalent frame model of masonry buildings. In addition to the material properties, the geometry is parametrized as well and thus, the model is representative of typical building structures, while the target domain is a real-world monitored structure, in this case a reinforced-concrete frame with masonry infill walls tested on a shake table (Figure 31).

A main ingredient of the proposed approach lies in the development of an extensive dataset of non-linear dynamic simulations. As aforementioned, we choose masonry buildings for our illustrations, as these comprise a characteristic building typology in Switzerland. A similar framework can be cast for moment frame structures that are representative of steel or reinforced concrete building systems. Multiple DSFs are computed based on ambient vibrations that would be monitored after an earthquake and ML classifiers are trained, able to fuse multiple DSFs into unified and robust damage indicators.

In order to enhance the generalization of the knowledge obtained from training on simulated systems to real structures, a domain-adaptation framework is proposed. As demonstrated in Figure 30, the proposed framework is trained on simulations and adapted to the new domain with limited data from the actual monitored structure (of interest), extracted from its healthy (or baseline) state. A Domain-Adversarial Neural Network approach (DANN) is deployed (Ganin & Lempitsky, 2015), which capitalizes on Generative Adversarial Networks (Goodfellow et al., 2014).

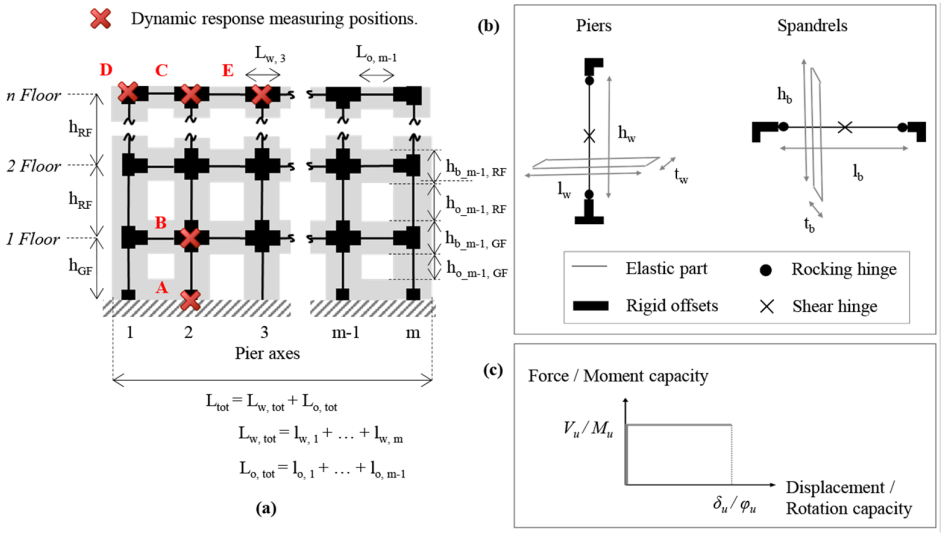

Figure 29 Equivalent frame model: (a) Generic representation of the parametric model, (b) Discretization and non-linear hinge positions, (c) Backbone curve formulation for the nonlinear hinges.

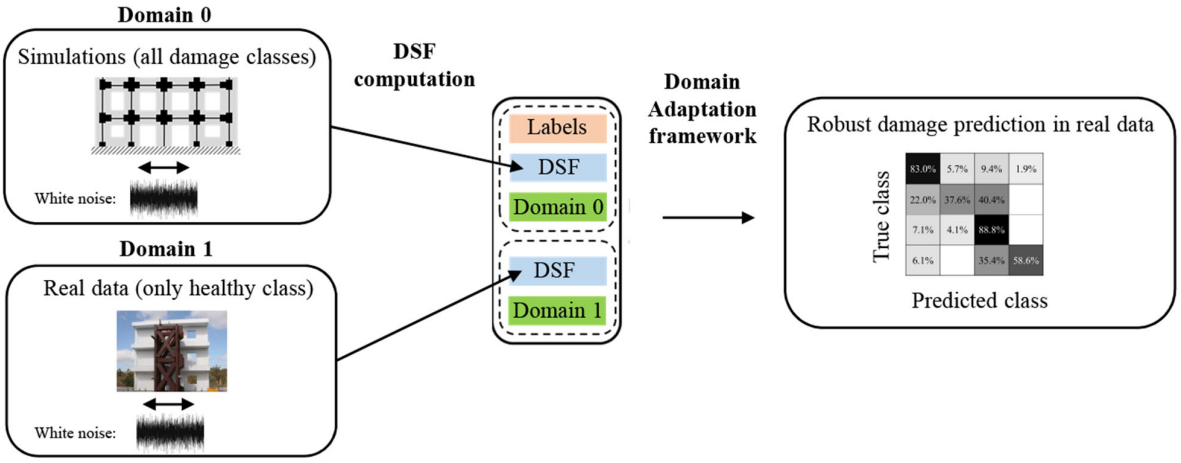

Figure 30 Overview of the domain adaptation framework for robust damage prediction in real structures, based on simulations and on limited healthy data from the monitored structure.

The performance of the developed domain adaptation scheme is evaluated on experimental data from a large-scale masonry-infilled RC frame. The structure, tested by (Stavridis et al., 2012), forms a two-dimensional three-floor frame structure and thus, complies with the modelled geometries considered by the simulator. However, the tested system comprises a material that is significantly different to the developed numerical simulator. The experimental system consists of RC frames and infill walls, while the parametrized numerical model was developed to represent URM shear-wall buildings. Domain adaptation is thus exemplified on a challenging case of discrepancy between the simulated training set and the real building, on which damage classification is attempted.

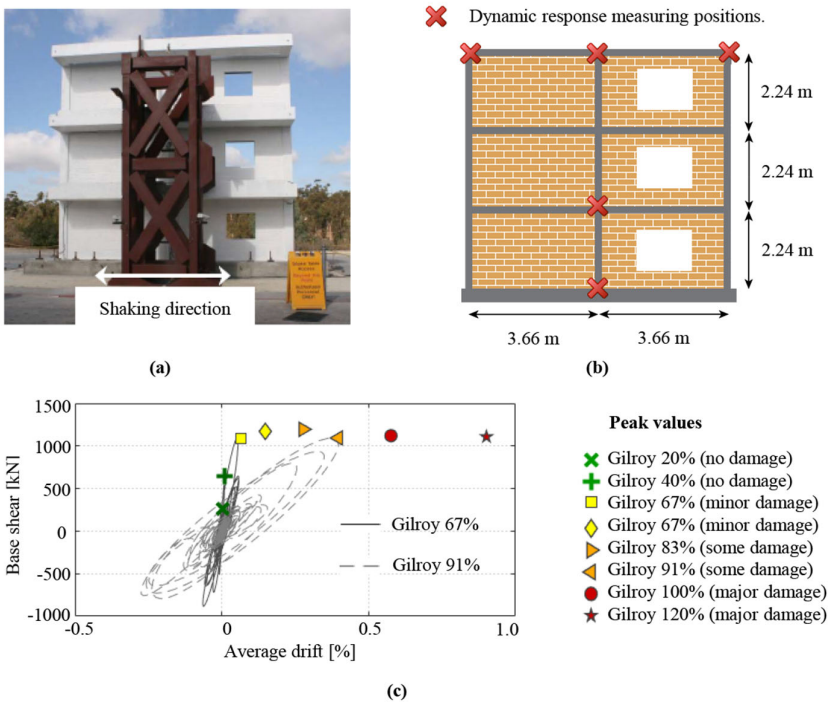

Figure 31 Overview of the test specimen and dynamic tests: (a) photo of the tested specimen, (b) summary of sensor locations used to derive DSFs and dimensions of the specimen, (c) backbone curve of the peak displacements and corresponding base force, together with the response-history of two ground motions.

The experimental structure was excited with the ground motion recorded during the 1989 Loma Prieta earthquake, which was scaled to increasing amplitudes; see (Stavridis et al., 2012) for a more thorough description of the experimental campaign.

Damage classification is performed for eight tests, with intensities ranging from 20% to 120% of the original earthquake. The measured acceleration signals at five locations marked in Figure 31b are used to compute the DSFs outlined in Section 3.

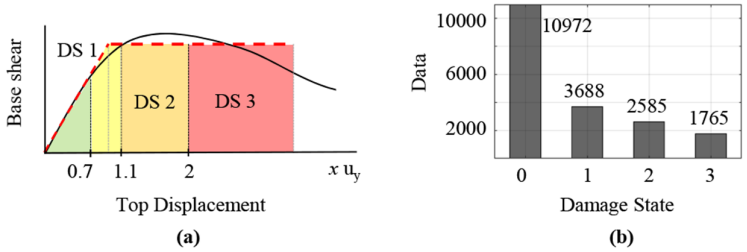

Figure 32 (a) Definition of empirical damage states on the basis of a bilinear approximation of a generic push-over curve, (b) Damage-state distribution of the dataset

The damage state observed on the specimen after each earthquake is also reported in Figure 31c. Given the damage state is based on observations and qualitative assessment, the damage states may not fully correspond to the definition used in the numerical simulations and outlined in Figure 32a. Yet, they reflect realistic conditions. Following each earthquake motion, the structure was subjected to WN excitations that are used here to derive the DSFs.

Damage prediction with pre-trained classifiers

As a reference point, the predictive performance of the ML algorithms, pre-trained on simulation data is evaluated on the experimental data. Two classifiers, the XGBoost (Chen & Guestrin, 2016), which is based on the gradient boosted decision trees (Friedman, 2001) parallelizing the training of multiple decision trees, and convolutional neural networks (CNN) are tested on the DSFs derived from the WN excitation in different damage states. The test data are segmented into 10-second windows, yielding a total of 567 labeled datapoints comprising 261 DS 0 (46%), 109 DS 1 (19%), 98 DS 2 (17%), and 99 DS 3 (17%).

As explained in the subsequent section, 50% of the healthy experimental data are used to train the domain adaptation network. In order to keep the same test set for the supervised and the DANN architectures, 50% of the healthy data, labeled as DS 0, are excluded from the test set, as they are used to train the DANN. Figure 33a and b visualize the predictive performance of the pre-trained networks, when exposed to the experimental data (target domain). The XGBoost architecture achieves an absolute accuracy of 58% and a soft accuracy (which accepts a misclassification by +/- 1 class) of 89%. The confusion matrix exposes a significant bias towards the predicted class 3 (DS 2), while the network shows poor performance in separating the healthy data (class 1 and 2) from the damaged classes. The performance of the CNN network is significantly worse, achieving an absolute accuracy of 25% and a soft accuracy of 77%. Again, there is a clear bias with respect to predicted class 3. These results expose the inability of pre-trained networks to generalize their predictive performance in domains that differ significantly from the training set. Indeed, ML classifiers over-fit to the source domain (simulations) and thus, cannot adapt to the target domain, which in this application differs from the source domain in terms of material (concrete vs simulated masonry), boundary conditions (in-filled walls) and origin (simulations vs experimental data with inherent noise).

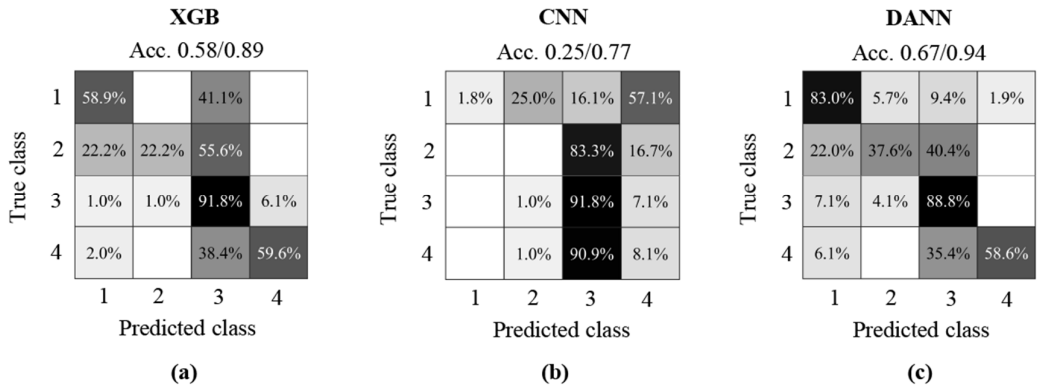

Figure 33 Predictive performance of Machine learning algorithms in the target domain: (a) pre-trained XGBoost, (b) pre-trained CNN and (c) DANN.

Damage prediction with domain adaptation

Domain adaptation aims to improve the predictive performance of a classifier in the target domain, for which only limited data, referring exclusively to the healthy state of the structure, are available. The developed DANN architecture is deployed, comprising three elements: a latent-space feature-extractor, a damage-classifier, and a domain-discriminator. Apart from the common training set containing the simulation data, 50% of the healthy data from the target domain (DS 0) are considered for training, without providing the label of their damage state. Finally, a binary domain label is provided: 0 for the source domain and 1 for the target domain.

The absolute accuracy of the DANN framework reaches 67% and a soft accuracy of 94% (Figure 33c), indicating significant improvement compared to the pre-trained networks. The DANN separates successfully the healthy class (DS 0) from damaged classes; and discriminates heavy damage classes (DS 2 and 3) from minor damage (DS 0 and 1). The prediction of DS 1 is only in 37.6% of the cases correct, although the confusion is limited to ±1 damage states. The definition of the damage in the experimental data was based on visual observations and involved qualitative evaluations of the damage state based on four empirical levels, namely "no damage", "minor damage", "some damage" and "major damage". Similar qualitative levels have been adopted for the formulation of the damage thresholds in the simulation data. Although the hard assumptions for the damage state thresholds do not directly affect the healthy state and the severe damaged states, DS 1 and DS 2 are sensitive to the exact values of the thresholds and the assumptions made when deriving the equivalent yield point. Thus, the observed uncertainty in predicting DS 1, as well as the partial confusion between DS 2 and 3 are deemed acceptable.

Overall, the deployed domain adaptation framework yields satisfactory results in predicting the damage state in the target domain, from which very limited and unlabelled data have been used for training. By comparing the performance of the DANN with the corresponding pre-trained CNN, sharing the same architecture in the feature-extractor and the damage-classifier segments, a significant improvement in prediction accuracy is achieved. The limited information from the experiments, which does not contain any data from damaged configurations, allows the DANN network to adapt successfully to the target domain. These results demonstrate the potential of DANN to transfer knowledge from numerical simulations into real-world monitoring applications.

6. Concluding remarks

Within WP4, Task 4.4, structural-health monitoring techniques have been extended and newly developed for post-seismic safety tagging of buildings, in support of rapid loss assessment. These techniques have been packed into a demonstrator (in MATLAB code), which can be exploited by the community as a baseline tool for RLA. The derived data-informed tags may be issued to building users and offer guidance to inspectors and first responders in near-real time and thus, presents a significant improvement with respect to current post-earthquake inspection practices that heavily rely on visual inspections. Fragility curves have been formulated with respect to damage-sensitive features that contain information about the building response during the earthquake and thus, may improve upon current fragility curves that rely only on intensity measure that characterize the ground-motion, without compromising on the regional applicability of such fragility curves.

The conclusions from formulating, demonstrating, and validating SHM-based post-earthquake building tagging are as follows:

- SHM provides precise information about an individual structure that has been instrumented with sensors. Such sensor information – even when taken alone – is found useful in providing information about the presence of damage and the evolution of damage over time, for instance throughout several earthquakes within a seismic sequence.
- With a simplified multi-degree-of-freedom model, DSF-based fragility curves are derived and used for a measured building response when undergoing a shake-table test. The predicted damage tags are coherent with the observations from the real structure, indicating the potential of SHM-based damage tagging, even when relying on simplified building models that may be used at regional scale.
- Physics-based models are required to enrich the available datasets to train damage classifiers or establish DSF-based fragility curves. To increase the robustness with respect to approximate and simplified models, a domain-adaptation methodology for machine-learning-based damage classification has been tested and is found to reduce classification errors that are committed when using diverging model and damage-state formulations. Only limited amounts of healthy data are required to adapt the classifier to the domain of real buildings, showing potential for installation after foreshocks or first earthquakes within a sequence, momentarily increasing the sensing capacities and thus, the number of buildings that may be tagged automatically after subsequent shocks.

7. References

Abdeljaber, O., Avci, O., Kiranyaz, S., Gabbouj, M., & Inman, D. J. (2017). Real-time vibration-based structural damage detection using one-dimensional convolutional neural networks. *Journal of Sound and Vibration*, *388*, 154–170. https://doi.org/10.1016/J.JSV.2016.10.043

Akhlaghi, M. M., Bose, S., Mohammadi, M. E., Moaveni, B., Stavridis, A., & Wood, R. L. (2021). Post-earthquake damage identification of an RC school building in Nepal using ambient vibration and point cloud data. *Engineering Structures*, *227*, 111413. https://doi.org/10.1016/J.ENGSTRUCT.2020.111413

Astorga, A., Guéguen, P., & Kashima, T. (2018). Nonlinear Elasticity Observed in Buildings during a Long Sequence of Earthquakes. *Bulletin of the Seismological Society of America*, *108*(3A), 1185–1198. https://doi.org/10.1785/0120170289

Atamturktur, S., & Laman, J. A. (2012). Finite element model correlation and calibration of historic masonry monuments: review. *The Structural Design of Tall and Special Buildings*, *21*(2), 96–113. https://doi.org/10.1002/tal.577

Avci, O., Abdeljaber, O., Kiranyaz, S., Hussein, M., Gabbouj, M., & Inman, D. J. (2021). A review of vibration-based damage detection in civil structures: From traditional methods

to Machine Learning and Deep Learning applications. *Mechanical Systems and Signal Processing*, *147*, 107077. https://doi.org/10.1016/j.ymssp.2020.107077

Azimi, M., Eslamlou, A., & Pekcan, G. (2020). Data-Driven Structural Health Monitoring and Damage Detection through Deep Learning: State-of-the-Art Review. *Sensors*, *20*(10), 2778. https://doi.org/10.3390/s20102778

Basseville, M., Mevel, L., & Goursat, M. (2004). Statistical model-based damage detection and localization: subspace-based residuals and damage-to-noise sensitivity ratios. *Journal of Sound and Vibration*, *275*(3–5), 769–794. https://doi.org/10.1016/j.jsv.2003.07.016

Beyer, K., Tondelli, M., Petry, S., & Peloso, S. (2015). Dynamic testing of a four-storey building with reinforced concrete and unreinforced masonry walls: prediction, test results and data set. *Bulletin of Earthquake Engineering*, *13*(10), 3015–3064. https://doi.org/10.1007/s10518-015-9752-z

Bodenmann, L., Reuland, Y., & Stojadinovic, B. (2021). Dynamic Updating of Building Loss Predictions Using Regional Risk Models and Conventional Post-Earthquake Data Sources. *Proceedings of the 31st European Safety and Reliability Conference*. https://doi.org/10.3929/ethz-b-000507866

Bodenmann, L., Reuland, Y., & Stojadinovic, B. (2022). Using Gaussian Process Models for Dynamic Post-Earthquake Impact Estimation with Regional Risk Predictors. *Bulletin of Earthquake Engineering*, *submitted*.

Bull, L. A., Gardner, P. A., Dervilis, N., Papatheou, E., Haywood-Alexander, M., Mills, R. S., & Worden, K. (2021). On the transfer of damage detectors between structures: An experimental case study. *Journal of Sound and Vibration*, *501*, 116072. https://doi.org/10.1016/j.jsv.2021.116072

Capsoni, A., & Moghadasi Faridani, H. (2016). Novel continuum models for coupled shear wall analysis. *The Structural Design of Tall and Special Buildings*, *25*(10), 444–467. https://doi.org/10.1002/tal.1267

Carden, E. P., & Fanning, P. (2004). Vibration Based Condition Monitoring: A Review. *Structural Health Monitoring*, *3*(4), 355–377. https://doi.org/10.1177/1475921704047500

Chen, T., & Guestrin, C. (2016). XGBoost. *Proceedings of the 22nd ACM SIGKDD International Conference on Knowledge Discovery and Data Mining*, 785–794. https://doi.org/10.1145/2939672.2939785

Crowley, H., Özcebe, S., Spence, R., Foulser-Piggott, R., Erdik, M., & Alten, K. (2012, September). Development of a European building inventory database. *Proceedings of the 15th World Conference on Earthquake Engineering*.

Farrar, C. R., & Worden, K. (2006). An introduction to structural health monitoring. *Philosophical Transactions of the Royal Society A: Mathematical, Physical and Engineering Sciences*, *365*(1851), 303–315. https://doi.org/10.1098/RSTA.2006.1928

Friedman, J. H. (2001). Greedy function approximation: A gradient boosting machine. *The Annals of Statistics*, *29*(5). https://doi.org/10.1214/aos/1013203451

Galloway, B., Hare, J., Brunsdon, D., Wood, P., Lizundia, B., & Stannard, M. (2019). Lessons from the Post-Earthquake Evaluation of Damaged Buildings in Christchurch: *Earthquake Spectra*, *30*(1), 451–474. https://doi.org/10.1193/022813EQS057M

Ganin, Y., & Lempitsky, V. (2015). Unsupervised domain adaptation by backpropagation. *International Conference on Machine Learning*, 1180–1189.

Gentile, C., Guidobaldi, M., & Saisi, A. (2016a). One-year dynamic monitoring of a historic tower: damage detection under changing environment. *Meccanica*, *51*(11), 2873–2889. https://doi.org/10.1007/s11012-016-0482-3

Gentile, C., Guidobaldi, M., & Saisi, A. (2016b). One-year dynamic monitoring of a historic tower: damage detection under changing environment. *Meccanica*, *51*(11), 2873–2889. https://doi.org/10.1007/s11012-016-0482-3

Giordano, P. F., & Limongelli, M. P. (2020). Response-based time-invariant methods for damage localization on a concrete bridge. *Structural Concrete*, *21*(4), 1254–1271. https://doi.org/10.1002/suco.202000013

Giordano, P. F., Quqa, S., & Limongelli, M. P. (2021). Statistical Approach for Vibration-Based Damage Localization in Civil Infrastructures Using Smart Sensor Networks. *Infrastructures*, *6*(2), 22. https://doi.org/10.3390/infrastructures6020022

Goodfellow, I., Pouget-Abadie, J., Mirza, M., Xu, B., Warde-Farley, D., Ozair, S., Courville, A., & Bengio, Y. (2014). Generative adversarial nets. *Advances in Neural Information Processing Systems*, *14*.

Goulet, J. A., Michel, C., & Kiureghian, A. der. (2015). Data-driven post-earthquake rapid structural safety assessment. Earthquake Engineering & Structural Dynamics, 44(4), 549–562. https://doi.org/10.1002/eqe.2541

Hoelzl, C., Ancu, L., Grossmann, H., Ferrari, D., Dertimanis, V., & Chatzi, E. (2022). *Classification of Rail Irregularities from Axle Box Accelerations Using Random Forests and*

Convolutional Neural Networks (pp. 91–97). https://doi.org/10.1007/978-3-031-04122-8_11

Jaishi, B., & Ren, W.-X. (2006). Damage detection by finite element model updating using modal flexibility residual. *Journal of Sound and Vibration*, *290*(1–2), 369–387. https://doi.org/10.1016/j.jsv.2005.04.006

Johnson, T. J., & Adams, D. E. (2002). Transmissibility as a Differential Indicator of Structural Damage. *Journal of Vibration and Acoustics*, *124*(4), 634–641. https://doi.org/10.1115/1.1500744

Juang, J.-N., & Pappa, R. S. (1985). An eigensystem realization algorithm for modal parameter identification and model reduction. *Journal of Guidance, Control, and Dynamics*, *8*(5), 620–627. https://doi.org/10.2514/3.20031

Kaya, Y., Kocakaplan, S., & Şafak, E. (2015). System identification and model calibration of multi-story buildings through estimation of vibration time histories at non-instrumented floors. *Bulletin of Earthquake Engineering*, *13*(11), 3301–3323. https://doi.org/10.1007/s10518-015-9774-6

Kita, A., Cavalagli, N., Masciotta, M. G., Lourenço, P. B., & Ubertini, F. (2020). Rapid post-earthquake damage localization and quantification in masonry structures through multidimensional non-linear seismic IDA. *Engineering Structures*, *219*, 110841. https://doi.org/10.1016/j.engstruct.2020.110841

Kita, A., Cavalagli, N., Venanzi, I., & Ubertini, F. (2021). A new method for earthquake-induced damage identification in historic masonry towers combining OMA and IDA. *Bulletin of Earthquake Engineering*, *19*(12), 5307–5337. https://doi.org/10.1007/s10518-021-01167-0

Kullback, S., & Leibler, R. A. (1951). On Information and Sufficiency. *The Annals of Mathematical Statistics*, *22*(1), 79–86.

Lagomarsino, S., & Cattari, S. (2015). *Seismic Performance of Historical Masonry Structures Through Pushover and Nonlinear Dynamic Analyses* (pp. 265–292). https://doi.org/10.1007/978-3-319-16964-4_11

Lagomarsino, S., & Giovinazzi, S. (2006). Macroseismic and mechanical models for the vulnerability and damage assessment of current buildings. *Bulletin of Earthquake Engineering*, *4*(4), 415–443. https://doi.org/10.1007/s10518-006-9024-z

Limongelli, M. P. (2014). Seismic health monitoring of an instrumented multistory building using the interpolation method. *Earthquake Engineering & Structural Dynamics*, *43*(11), 1581–1602. https://doi.org/10.1002/eqe.2411

Lorenzoni, F., Caldon, M., da Porto, F., Modena, C., & Aoki, T. (2018). Post-earthquake controls and damage detection through structural health monitoring: applications in l'Aquila. *Journal of Civil Structural Health Monitoring*, *8*(2), 217–236. https://doi.org/10.1007/S13349-018-0270-Y/FIGURES/16

Luo, Z., Liu, H., & Yu, L. (2021). Weighted Transmissibility Assurance Criterion for Structural Damage Detection. *Journal of Aerospace Engineering*, *34*(3). https://doi.org/10.1061/(ASCE)AS.1943-5525.0001251

Mangalathu, S., Sun, H., Nweke, C. C., Yi, Z., & Burton, H. v. (2020). Classifying earthquake damage to buildings using machine learning. *Earthquake Spectra*, *36*(1), 183–208. https://doi.org/10.1177/8755293019878137

Martakis, P., Reuland, Y., & Chatzi, E. (2021a). Amplitude-dependent model updating of masonry buildings undergoing demolition. *Smart Structures and Systems*, *27*(2), 157–172.

Martakis, P., Reuland, Y., & Chatzi, E. (2021b). Amplitude-dependent model updating of masonry buildings undergoing demolition. *Smart Structures and Systems*, *27*(2), 157–172. https://doi.org/10.12989/SSS.2021.27.2.157

Martakis, P., Reuland, Y., & Chatzi, E. (2022). Amplitude Dependency Effects in the Structural Identification of Historic Masonry Buildings. In C. Pellegrino, F. Faleschini, M. A. Zanini, J. C. Matos, J. R. Casas, & A. Strauss (Eds.), *Proceedings of the 1st Conference of the European Association on Quality Control of Bridges and Structures. EUROSTRUCT 2021.* (Vol. 200, pp. 140–147). Springer, Cham. https://doi.org/10.1007/978-3-030-91877-4_17

Martakis, P., Reuland, Y., Imesch, M., & Chatzi, E. (2022). Reducing uncertainty in seismic assessment of multiple masonry buildings based on monitored demolitions. *Bulletin of Earthquake Engineering*, *20*(9), 4441–4482. https://doi.org/10.1007/s10518-022-01369-0

Martins, L., & Silva, V. (2021). Development of a fragility and vulnerability model for global seismic risk analyses. *Bulletin of Earthquake Engineering*, *19*(15), 6719–6745. https://doi.org/10.1007/s10518-020-00885-1

Mazzoni, S., McKenna, F., Scott, M. H., & Fenves, G. L. (2006). *OpenSees Command Language Manual*. University of California, Berkeley.

Mcentire, D. A., & Cope, J. (2004). *Damage Assessment After the Paso Robles (San Simeon, California) Earthquake: Lessons for Emergency Management*.

McKenna, F., Scott, M. H., & Fenves, G. L. (2010). Nonlinear Finite-Element Analysis Software Architecture Using Object Composition. *Journal of Computing in Civil Engineering*, *24*(1), 95–107. https://doi.org/10.1061/(ASCE)CP.1943-5487.0000002

Michel, C., Zapico, B., Lestuzzi, P., Molina, F. J., & Weber, F. (2011). Quantification of fundamental frequency drop for unreinforced masonry buildings from dynamic tests. *Earthquake Engineering & Structural Dynamics*, *40*(11), 1283–1296. https://doi.org/10.1002/eqe.1088

Movsessian, A., Cava, D. G., & Tcherniak, D. (2022). Interpretable Machine Learning in Damage Detection Using Shapley Additive Explanations. *ASCE-ASME J Risk and Uncert in Engrg Sys Part B Mech Engrg*, *8*(2). https://doi.org/10.1115/1.4053304

Noh, H. Y., Asce, S. M., Krishnan Nair, ; K, Lignos, D. G., Asce, A. M., Kiremidjian, A. S., & Asce, M. (2011). Use of Wavelet-Based Damage-Sensitive Features for Structural Damage Diagnosis Using Strong Motion Data. *Journal of Structural Engineering*, *137*(10), 1215–1228. https://doi.org/10.1061/(ASCE)ST.1943-541X.0000385

Orlacchio, M., Chioccarelli, E., Baltzopoulos, G., & Iervolino, I. (2021). State-dependent seismic fragility functions for Italian reinforced concrete structures: preliminary results. *31st European Safety and Reliability Conference - ESREL 2021*.

Ou, Y., Chatzi, E. N., Dertimanis, V. K., & Spiridonakos, M. D. (2016). Vibration-based experimental damage detection of a small-scale wind turbine blade: *Structural Health Monitoring*, *16*(1), 79–96. https://doi.org/10.1177/1475921716663876

Pan, S. J., & Yang, Q. (2010). A Survey on Transfer Learning. *IEEE Transactions on Knowledge and Data Engineering*, *22*(10), 1345–1359. https://doi.org/10.1109/TKDE.2009.191

Pina Limongelli, M., Chatzi, E., Döhler, M., Lombaert, G., Pina LIMONGELLI, M., & Reynders, E. (2016). Towards extraction of vibration-based damage indicators. *EWSHM - 8th European Workshop on Structural Health Monitoring*. https://hal.inria.fr/hal-01344178

Reuland, Y., Bodenmann, L., Blagojevic, N., & Stojadinovic, B. (2022). *Deliverable 4.4 Development of RRE forecasting services in OpenQuake*.

Reuland, Y., Lestuzzi, P., & Smith, I. F. C. (2019a). A model-based data-interpretation framework for post-earthquake building assessment with scarce measurement data. *Soil Dynamics and Earthquake Engineering*, *116*, 253–263. https://doi.org/10.1016/j.soildyn.2018.10.008

Reuland, Y., Lestuzzi, P., & Smith, I. F. C. (2019b). Measurement-based support for post-earthquake assessment of buildings. *Structure and Infrastructure Engineering*, *15*(5), 647–662. https://doi.org/10.1080/15732479.2019.1569071

Roselli, I., Malena, M., Mongelli, M., Cavalagli, N., Gioffrè, M., de Canio, G., & de Felice, G. (2018). Health assessment and ambient vibration testing of the "Ponte delle Torri" of Spoleto during the 2016–2017 Central Italy seismic sequence. *Journal of Civil Structural Health Monitoring*, *8*(2), 199–216. https://doi.org/10.1007/s13349-018-0268-5

Rytter, A. (1993). *Vibration based inspection of civil engineering structures*. Aalborg University.

Salawu, O. S. (1997). Detection of structural damage through changes in frequency: a review. *Engineering Structures*, *19*(9), 718–723. https://doi.org/10.1016/S0141-0296(96)00149-6

Sheibani, M., & Ou, G. (2021). The development of Gaussian process regression for effective regional post-earthquake building damage inference. *Computer-Aided Civil and Infrastructure Engineering*, *36*(3), 264–288. https://doi.org/10.1111/MICE.12630

Sheibani, M., & Ou, G. (2022). Active Learning of Post-earthquake Structural Damage with Co-optimal Information Gain and Reconnaissance Cost. *Conference Proceedings of the Society for Experimental Mechanics Series*, 9–16. https://doi.org/10.1007/978-3-030-76004-5_2

Shokrani, Y., Dertimanis, V. K., Chatzi, E. N., & N. Savoia, M. (2018). On the use of mode shape curvatures for damage localization under varying environmental conditions. *Structural Control and Health Monitoring*, *25*(4), e2132. https://doi.org/10.1002/stc.2132

Sohn, H., Worden, K., & Farrar, C. R. (2002). Statistical Damage Classification Under Changing Environmental and Operational Conditions. *Journal of Intelligent Material Systems and Structures*, *13*(9), 561–574. https://doi.org/10.1106/104538902030904

Solís, M., Algaba, M., & Galvín, P. (2013). Continuous wavelet analysis of mode shapes differences for damage detection. *Mechanical Systems and Signal Processing*, *40*(2), 645–666. https://doi.org/10.1016/j.ymssp.2013.06.006

Song, M., Moaveni, B., Papadimitriou, C., & Stavridis, A. (2019). Accounting for amplitude of excitation in model updating through a hierarchical Bayesian approach: Application to a two-story reinforced concrete building. *Mechanical Systems and Signal Processing*, *123*, 68–83. https://doi.org/10.1016/j.ymssp.2018.12.049

Stavridis, A., Koutromanos, I., & Shing, P. B. (2012). Shake-table tests of a three-story reinforced concrete frame with masonry infill walls. *Earthquake Engineering & Structural Dynamics*, *41*(6), 1089–1108. https://doi.org/10.1002/eqe.1174

Stojadinović, Z., Kovačević, M., Marinković, D., & Stojadinović, B. (2022). Rapid earthquake loss assessment based on machine learning and representative sampling. *Earthquake Spectra*, *38*(1), 152–177. https://doi.org/10.1177/87552930211042393

Sun, L., Shang, Z., Xia, Y., Bhowmick, S., & Nagarajaiah, S. (2020). Review of Bridge Structural Health Monitoring Aided by Big Data and Artificial Intelligence: From Condition Assessment to Damage Detection. *Journal of Structural Engineering*, *146*(5). https://doi.org/10.1061/(ASCE)ST.1943-541X.0002535

Tatsis, K., Dertimanis, V., Abdallah, I., & Chatzi, E. (2017). A substructure approach for fatigue assessment on wind turbine support structures using output-only measurements. *Procedia Engineering*, *199*, 1044–1049. https://doi.org/10.1016/j.proeng.2017.09.285

Trevlopoulos, K., & Guéguen, P. (2016). Period elongation-based framework for operative assessment of the variation of seismic vulnerability of reinforced concrete buildings during aftershock sequences. Soil Dynamics and Earthquake Engineering, 84, 224–237. https://doi.org/10.1016/j.soildyn.2016.02.009

Tsuchimoto, K., Narazaki, Y., & Spencer, B. F. (2021). Development and Validation of a Post-Earthquake Safety Assessment System for High-Rise Buildings Using Acceleration Measurements. *Mathematics*, *9*(15), 1758. https://doi.org/10.3390/math9151758

van Overschee, P., & de Moor, B. (1996). Continuous-time frequency domain subspace system identification. *Signal Processing*, *52*(2), 179–194. https://doi.org/10.1016/0165-1684(96)00052-7

Vidal, F., Navarro, M., Aranda, C., & Enomoto, T. (2014). Changes in dynamic characteristics of Lorca RC buildings from pre- and post-earthquake ambient vibration data. *Bulletin of Earthquake Engineering*, *12*(5), 2095–2110. https://doi.org/10.1007/S10518-013-9489-5/TABLES/3

Villar-Vega, M., Silva, V., Crowley, H., Yepes, C., Tarque, N., Acevedo, A. B., Hube, M. A., Gustavo, C. D., & María, H. S. (2017). Development of a Fragility Model for the Residential Building Stock in South America. *Earthquake Spectra*, *33*(2), 581–604. https://doi.org/10.1193/010716EQS005M

Wald, D. J., Quitoriano, V., Heaton, T. H., Kanamori, H., Scrivner, C. W., & Worden, C. B. (1999). TriNet "ShakeMaps": Rapid Generation of Peak Ground Motion and Intensity Maps for Earthquakes in Southern California. *Earthquake Spectra*, *15*(3), 537–555. https://doi.org/10.1193/1.1586057

Worden, C. B., Thompson, E. M., Baker, J. W., Bradley, B. A., Luco, N., & Wald, D. J. (2018). Spatial and Spectral Interpolation of Ground-Motion Intensity Measure Observations. *Bulletin of the Seismological Society of America*, *108*(2), 866–875. https://doi.org/10.1785/0120170201

Xu, S., & Noh, H. Y. (2019, November 15). Knowledge Transfer Between Buildings for Post-Earthquake Damage Diagnosis Without Historical Data. *Structural Health Monitoring 2019*. https://doi.org/10.12783/shm2019/32141

Young Noh, H., Krishnan Nair, K., Lignos, D. G., & Kiremidjian, A. S. (2011). Use of Wavelet-Based Damage-Sensitive Features for Structural Damage Diagnosis Using Strong Motion Data. *Journal of Structural Engineering*, *137*(10), 1215–1228. https://doi.org/10.1061/(ASCE)ST.1943-541X.0000385

Zhou, Y.-L., Cao, H., Liu, Q., & Wahab, M. A. (2017). Output-Based Structural Damage Detection by Using Correlation Analysis Together with Transmissibility. *Materials*, *10*(8), 866. https://doi.org/10.3390/ma10080866